

# **Oceanic gateways in Antarctica - Impact Bathymetry-constrained impact of relative sea-level change on sub-shelf meltbasal melting in Antarctica**

Moritz Kreuzer<sup>1,2</sup>, Torsten Albrecht<sup>1</sup>, Lena Nicola<sup>1,2</sup>, Ronja Reese<sup>3,1</sup>, and Ricarda Winkelmann<sup>1,2</sup>

<sup>1</sup> Potsdam Institute for Climate Impact Research (PIK), Member of the Leibniz Association, P.O. Box 601203, D-14412 Potsdam, Germany

<sup>2</sup> University of Potsdam, Institute of Physics and Astronomy, Karl-Liebknecht-Str. 24-25, D-14476 Potsdam, Germany

<sup>3</sup> Department of Geography and Environmental Sciences, Northumbria University, Ellison Place, NE1 8ST, Newcastle Upon Tyne, UK

**Correspondence:** Moritz Kreuzer (kreuzer@pik-potsdam.de)

**Abstract.** Relative sea level (local water depth) on the Antarctic ~~continental shelf~~ continent is changing by the complex interplay of processes associated with Glacial Isostatic Adjustment (GIA). This involves near-field visco-elastic bedrock displacement and ~~self-gravitational~~ gravitational effects in response to changes in Antarctic ice load, but also far-field interhemispheric effects on the sea-level pattern. On glacial time scales, these changes can be in the order of several hundred meters, modulating

5 potentially affecting the access of ocean water masses at different depths to Antarctic grounding lines. Our study shows that due and ice-sheet margins. Due to strong vertical gradients in ocean temperature and salinity at the continental shelf margin, basal melt rates of ice shelves can change significantly have the potential to change just by variations in relative sea level alone. Based on simulated relative sea-level change from coupled ice sheet – GIA model experiments and the analysis of topographic features such as troughs and sills that regulate the access of open ocean water masses onto the continental shelf (oceanic

10 gateways), we derive maximum estimates of Antarctic basal melt rate changes, solely driven by relative sea-level variations.

Under Last Glacial Maximum Our results suggest that the effect of relative sea-level conditions, this effect would lead to a substantial decrease of present-day sub-shelf melt rates in East Antarctica, while the strong subsidence of bedrock in West Antarctica can lead up to a doubling of basal melt rates. For a hypothetical globally ice-free sea-level scenario, which would lead to a global mean (barystatic) sea-level rise of around +70, sub-shelf melt rates for a present-day ice sheet geometry can 15 more than double in East Antarctica, but can also decrease substantially, where bedrock uplift dominates. Also for projected sea-level changes at the year 2300 we find maximum possible changes of  $\pm 20\%$  in sub-shelf melt rates, as a consequence of relative sea-level changes only changes on basal melting is limited, especially compared to transient changes in the climate forcing.

## 1 Introduction

20 Global-mean sea level (GMSL) varies on glacial-interglacial time scales in the order of 100 m depending on the density of ocean water (steric effects) and the total ocean area, which. The dominant component of GMSL changes since the Last

Glacial Maximum (LGM, ca. 21 kyr BP; Gebbie, 2020) is determined by the mass redistribution between ocean and land (e.g. by ice sheet changes; Miller et al., 2020; Horwath et al., 2022). ~~The latter component is also, which is~~ referred to as *barystatic sea-level change* (Gregory et al., 2019), ~~and is the dominant component of GMSL changes since the Last Glacial Maximum (LGM, ca. 21 kyr BP; Gebbie, 2020)~~. Changes in ocean density (steric effects) play only a minor role on glacial time scales, but have a relevant contribution to anthropogenic sea-level rise (Gebbie, 2020; Marcos and Amores, 2014). The global distribution of ~~the~~ sea level aligns according to an equipotential surface, also called the *geoid* (Gregory et al., 2019), which is determined by the gravity field of ice, water and the Earth's mantle material, with a feedback on Earth's rotation (Mitrovica et al., 2005). Variations of sea-level height through ocean currents and winds are not ~~covered by~~ ~~included in~~ the geoid definition. The *relative sea level* (RSL) is the depth of the water column, hence the vertical distance between the geoid and the ocean bathymetry (or when negative, the land surface elevation above the geoid), and it can change through several processes:

1. *Changes in ice masses* affect the volume and area of the global ocean, leading to a globally distributed, barystatic shift of the geoid height.
2. The mass redistribution between ice and ocean also affects the Earth's *rotational* axis, such that the global sea-level ~~pattern~~ ~~fingerprint~~ adjusts to the change in centrifugal acceleration.
3. The *gravitational* force exerted by ice masses on the surrounding ocean masses leads to variations in local geoid height near ice sheets ~~when there is a gain or loss~~ ~~following gains or losses~~ of ice mass.
4. Changes in load have *deformational* (visco-elastic) effects on the solid Earth, leading to subsidence or uplift of the underlying bedrock topography. ~~This causes a horizontal flux of mantle material as well as an elastic response of the lithosphere. The reverse~~ ~~Due to the flexure of the lithospheric plate and the viscous flow of upper mantle material, an increase in ice load would therefore produce an uplift at some distance from the centre of the load, yielding a reversed (negative) signal in RSL, which occurs in the vicinity with smaller magnitude~~; ~~this~~ is called a 'forebulge'. Depending on the local mantle viscosity and lithosphere thickness, ~~this~~ ~~these~~ visco-elastic ~~process~~ ~~processes~~ can induce vertical changes of hundreds of meters.

These mechanisms act on different spatial and temporal scales, i.e. almost instantaneous in case ~~of~~ of rotational and gravitational effects, whereas bedrock deformation can take several millennia to unfold. All of the mentioned mechanisms are covered by the *Glacial Isostatic Adjustment* theory (GIA; Farrell and Clark, 1976; Whitehouse, 2018). Global mean sea level is also influenced by thermosteric effects through changes in ocean water temperature, but this effect is comparably small on glacial time scales.

During the Last Glacial Maximum, GMSL was about 125–134 m lower than today, mainly due to the greater extent of northern hemisphere ice sheets (Yokoyama et al., 2018; Lambeck et al., 2014). Grounded ice in Antarctica reached close

to the continental-shelf break (CSB) in many locations during the LGM (Bentley et al., 2014) and holding up to 20 m sea-level equivalent more ice, according to the literature review in Albrecht et al. (2020b, Fig. 11b). Today's configuration of the Antarctic Ice Sheet (AIS) still holds enough ice to raise GMSL by approx. 58 m if melted completely (neglecting isostatic or thermal effects; Morlighem et al., 2020). Considering all land-based ice on Earth, including the Greenland Ice Sheet and mountain glaciers, this number increases to approx. 66 m (IPCC AR6 WG1 Ch. 2.3.3.3, Gulev et al., 2021).

While Antarctic ice mass changes have been small in the Late Holocene (approx. last 4000 years, Jones et al., 2022), the AIS is losing mass at an increasing rate in the last decades (Shepherd et al., 2012; Rignot et al., 2019; Otosaka et al., 2023). Due to ongoing atmospheric and ~~ocean~~oceanic warming, it is projected that Antarctica loses up to 3.133.1 m of sea-level equivalent ice volume by 2300 under a high-emission scenario (IPCC AR6 WG1 Ch. 9.6.3.5, Fox-Kemper et al., 2021). When considering the long-term stability of the ice sheet, Garbe et al. (2020) find that due to several feedback mechanisms, the AIS is bound to become ice-free at warming greater than 10 °C above pre-industrial levels.

65 Melting of ice shelves, the floating extensions of the marine ice sheets, is highly sensitive to changes in ocean temperatures on the continental shelf, especially when warm water masses intrude into the ice-shelf cavities at depth (Hellmer et al., 2012; Pritchard et al., 2016)  
. Sub-shelf melt rates are generally highest close to the grounding line, where grounded ice becomes afloat (Rydt and Gudmundsson, 2016)  
. For ice-sheet simulations over long time scales, such as glacial cycles, climatic boundary conditions as ocean and atmospheric temperature have to be parameterized in a robust manner. Albrecht et al. (2020a) use a temperature-index method and linear  
70 response functions to scale present-day ocean temperature observations on the continental shelf, which is the shallow ocean area surrounding the Antarctic Ice Sheet, with climatic variations derived from ice-core data. For shorter time scales, i.e. end-of-century projections, stand-alone ice sheet models are typically forced by the output of climate models (Seroussi et al., 2020)

75 In order to assess the stability and long-term behaviour of ice sheets, interactions with the solid Earth and sea level are relevant as GIA responses can have major feedbacks on with ice dynamics (Whitehouse et al., 2019). Albrecht et al. (2023, in prep.)  
Albrecht et al. (2023, accepted), for instance, use a globally consistent coupled ice sheet – GIA model framework and find that ice retreat can be significantly slowed down when isostatic rebound is included, in particular when considering a weak Earth structure with low mantle viscosity and thin lithosphere, as reconstructions suggest for the West Antarctic plate (Barletta et al., 2018)  
80 (Barletta et al., 2018; Bagge et al., 2021). Coupled ice sheet – GIA models exist in different modes of complexity, e.g. with regional setups (Coulon et al., 2021; Zeitz et al., 2022), 1-dimensional Earth structure (Pollard et al., 2017; Gomez et al., 2020) or globally 3-dimensional, which are just becoming available as in van Calcar et al. (2023) and Albrecht et al. (in prep. 2023)  
Gomez et al. (2018), van Calcar et al. (2023) and Albrecht et al. (2023, accepted).

85 For ice-sheet simulations over long time scales, such as glacial cycles, climatic boundary conditions as ocean and atmospheric temperature have to be parameterized in an appropriate way. Albrecht et al. (2020a) use a temperature-index method and linear response functions to scale present-day ocean temperature observations on the continental shelf, which is the shallow ocean area surrounding the Antarctic Ice Sheet, with climatic variations derived from ice-core data. A similar approach is taken by Chandler et al. (2023, in discuss.), which has been successfully tested against paleo reconstructions (Chandler and Langebroek, 2023, in discuss.)

90 . Melting of ice shelves, the floating extensions of the marine ice sheets, is highly sensitive to changes in ocean temperatures on the continental shelf, especially when warm water masses intrude into the GIA processes also influence ocean dynamics in various ways: Rugenstein et al. (2014) demonstrate that the presence of a forebulge, which rises the Southern Ocean floor by approx. 50 m in response to additional ice loading, can significantly alter ocean velocities, frontal structures and zonal transport. Wilmes et al. (2017) show that tides are affected by changes in RSL patterns. Tinto et al. (2019) argue that sub-shelf bathymetry controls the oceanic flow beneath the Ross Ice Shelf, which is subject to change due to GIA processes. Motivated 95 by these previous studies, the focus of our analysis is how RSL changes can influence basal melting in ice-shelf cavities at depth (Hellmer et al., 2012; Pritchard et al., 2012; Rintoul et al., 2016). Sub-shelf melt rates are generally highest.

100 Temperatures and salinities in the Southern Ocean show a strong dependence with depth: while surface waters are close to the grounding line, where grounded ice becomes afloat (Rydt and Gudmundsson, 2016). The grounding line position is determined by the RSL via the floatation condition. Hence, changes in RSL can affect the grounding line position and freezing point of seawater (ca.  $-1.9^{\circ}\text{C}$ ), temperatures increase with an average rate of  $+0.5^{\circ}\text{C}$  per 100 meters in the ice-sheet dynamics. In fact, changes in RSL can also influence the ocean forcing directly, which we discuss in the following:

105 *thermocline layer* (approx. upper 600 m) and decrease slowly below to reach about  $0^{\circ}\text{C}$  at 1800 m (see Fig. S1 in the supplementary material). Similarly, ocean salinities increase from about 34.0 psu (practical salinity unit) at the surface to ca. 34.7 psu at 600 m depth and stay rather constant below (see Fig. S2). The thermocline layer is characterised by the transition 110 between cold and fresh surface waters and warmer, saltier Circumpolar Deep Water (CDW). As (positive values of) RSL indicate the local water column depth, changes of RSL can be interpreted as a negative displacement of bedrock topography relative to the geoid. From an ice-sheet perspective the local sea level thus remains at the same reference elevation ( $z = 0$ ), whereas bedrock elevation is modulated according to changes in relative sea level. The change in bedrock provides potential 115 access to the continental shelf for water masses from different depths, assuming that bathymetry primarily controls flow. The upper layers of the Southern Ocean (approx. upper 600) show a strong increase of potential temperature with depth of about  $+0.5$  per 100 meters on average (see Fig. S4 in the Supplement). This *thermocline layer* is characterised by the transition between cold and fresh surface waters and warmer, saltier Circumpolar Deep Water (CDW). The typical depth of the continental shelf around Antarctica (approx. 500) is in the range of the thermocline layer, such that small RSL changes can have a 120 comparably large effect on the available ocean temperature and heat on the continental shelf, assuming no changes in flow pattern resulting from RSL changes. As depicted in Fig. 1, sea-level changes in the order of 100 meters can have significant impacts on the heat available for melting at the In a related study, Nicola et al. (2023b, in discuss.) show that bathymetry can play a crucial role in the interaction between the AIS and the surrounding ocean: topographic features such as troughs and sills can act as *oceanic gateways* through providing or blocking access of warm CDW into the ice-shelf base, even with no further climatic temperature changes or grounding line migration considered.

Furthermore, the cavities, from where it potentially reaches deep-lying grounding lines (Thoma et al., 2008; Nicholls et al., 2009; Hellmer et al., 2012). At the same time the pattern of RSL changes is highly dependent on the local GIA response to ice dynamics. Visco-elastic On glacial time scales, the near-field visco-elastic vertical displacement of bedrock as a consequence of a changing ice load

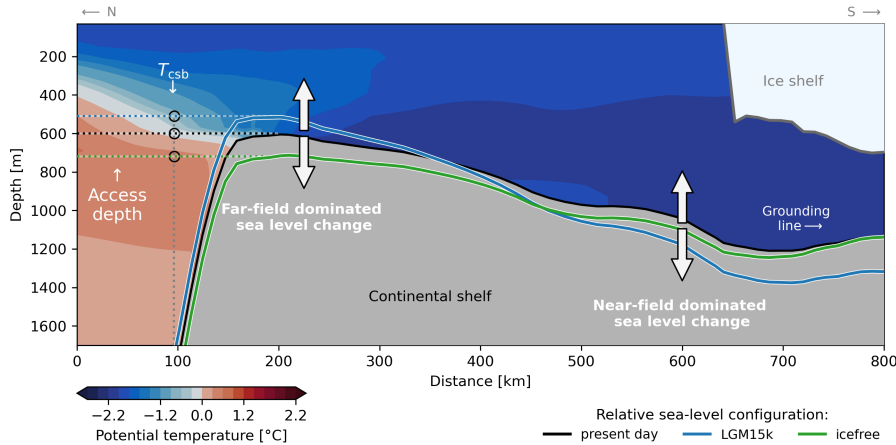


**Figure 1. Schematic of a typical oceanic gateway, where topography shields a deep-lying grounding line from warm-water inflow.** A transect following the deepest topographic connection (along a trough) shows a common temperature distribution for the Antarctic continental shelf. Variations of the sill depth can occur in response to far-field and near-field variations of relative sea-level, which affects the access depth from where offshore water masses flow onto the continental shelf. The effect of RSL changes on basal melt rates can be assessed by evaluating the change in ocean properties resulting from variations in access depths at the continental-shelf break ( $T_{\text{csb}}$ ).

and gravitational attraction can outweigh the barystatic ('far-field') sea-level signal and lead to several hundreds of meter

125 change in RSL, on glacial time scales. In a related study, Nicola et al. (2023b, subm.) show that bathymetry generally plays a crucial role in the interaction between the AIS and the surrounding ocean: topographic features such as troughs and sills act as *oceanic gateways* as they provide or block access of warm CDW into the ice-shelf cavities towards deep-lying grounding lines. A changing topography through regionally varying patterns of relative sea level thus has the potential to strongly influence basal melting in the ice-shelf.

130 The typical depth of the continental shelf around Antarctica (approx. 500 m) is in the range of the thermocline layer. Assuming that changes in bathymetry do not influence the horizontal circulation patterns between open ocean water masses (at the CSB or further offshore) and shallow water masses on the continental shelf, a change in RSL could give water masses from different depths access to the continental shelf and potentially into the cavities, where it would affect melting underneath the ice shelves. Within the thermocline layer, water properties at the CSB are getting colder and fresher when RSL decreases, 135 and warmer and saltier during an increase in RSL (cf. Fig. S1). Figure 1 shows a schematic of this concept and also highlights the typical spatial pattern of RSL changes.

In this study, we investigate the potential influence

140 So far the effect of RSL changes on Antarctic basal melt rates has not been assessed. The importance and relevance of this effect is thus unclear and whether this mechanism should be considered for the ocean forcing in ice-sheet simulations. With this study we want to provide an approximate estimate on the potential impact of relative sea-level changes on Antarctic ice-shelf

change on basal melt rates in 19 individual basins around Antarctica, due to deformational, rotational or gravitational effects of GIA in response to the redistribution of masses between ice and ocean Antarctica. To our knowledge this effect has not been quantified so far. We therefore derive estimates for the maximum impact.

145 We first define different RSL configurations, which represent end-member realisations for past and future change in sea level, as well as an upper-end estimate for possible changes in the year 2300. From these RSL patterns we compute the change in open-ocean connectivity to grounding lines of the Antarctic Ice Sheet and infer how this changes the ocean properties that get access onto the continental shelf. By adding the derived changes in continent-shelf break temperature and salinities as anomalies to an ice-sheet model, we compute changes in basal melt rates based on the RSL signal.

150 The study consists of two different sets of experiments: In a first step, we test the sensitivity of a present-day ice-sheet configuration to end-member realisations of RSL change patterns to derive upper limit estimates of this effect, based on upper limit scenarios, but also assess the impact on time scales of the upcoming centuries. We explain the methodology of our analysis in Sect. 2, present the results in Sect. 3 and end with a discussion (Sect. 4) and conclusion of our results (Sect. 5) on basal melt rate changes. Secondly, we apply RSL driven ocean forcing corrections for specific past and future time slices of the Antarctic ice-sheet evolution to assess the effect of RSL-induced basal melt rates changes also in more realistic scenarios.

155 **Transect through Filehner Trough showing relevant terms and concepts used in this study.** The sill north of Filehner–Ronne Ice Shelf determines the critical access depth of the basin, indicated by dashed horizontal lines. Variations of the sill depth can occur in response to barystatic and far-field sea-level changes while the bathymetry within the ice-shelf cavity is mainly influenced by the near-field effects from GIA, which can induce an additional forbudge effect on sill depth. To assess the potential impact of those changes on sub-shelf melt, temperature and salinity (the latter indicated as white contour lines in unit psu) estimates from Jourdain et al. (2020) are evaluated at the critical access depth near the continental-shelf break, marked as  $T_{\text{csb}}$ ,  $S_{\text{csb}}$ . Magenta line in inlet map shows transect location.

## 2 Methods

160 This section describes the methods, scenarios and workflow we use to derive ice-shelf basal melt rate estimates from by applying different relative sea-level changes.

165 To derive upper limit estimates, the analysis is based on two ‘end-of-the-spectrum’ scenarios: (1) a global land–ice distribution. In order to assess the relevance and magnitude of relative sea-level on basal melt rates, we define different configurations of relative sea-level change. For an upper limit estimate of past RSL changes, we choose the maximum ice extent of the AIS during the Last Glacial Maximum with a global mean (barystatic) sea-level approx. 93 lower than today, and (2) a configuration with all continental ice masses transformed into liquid water (GMSL  $\approx +70$ ). In order to assess also near-future impacts, we add another scenario (3) based on a projection following the ISMIP6 Antarctica extensions until the, which is named *LGM15k* in the following. For an upper limit of expected future changes, we assume a configuration where all present-day solid ice is melted and the global mean sea-level as well as solid Earth rebound would thus be highest (*icefree*). For an intermediate and

175 more realistic future setup, we also assess a configuration in the year 2300 with a high emission scenario (SSP5-8.5). In the following we will refer to these scenarios as *LGM15k*, *icefree* and *yr2300*, which are described further below (See. ??, with the Antarctic Ice Sheet being forced by an upper limit climate projection (*yr2300*). More information about these configurations is given below (Sect. 2.1.2).

180 To estimate sub-shelf melt rate changes for the ~~scenarios mentioned above~~ different RSL configurations, we follow these steps:

1. Compute relative sea-level changes with coupled ice sheet–GIA simulations.
2. Identify ~~eritical access~~ depths informed by relative sea-level changes to determine open ocean access to ice-sheet grounding lines.
3. Calculate ocean state changes at the continental-shelf break ~~due to on the basis of~~ vertical displacement of ~~eritical access~~ depths.
4. Compute diagnostic changes in ice-shelf basal melt rates with an ice-sheet model.

~~The computation of RSL changes involves dynamic ice-sheet changes, while the rest of the analysis relies on a static, present-day configuration of the AIS and the surrounding ocean. Reasons and implications of this are further discussed in Sect. 4.~~ In the following, we explain the methodology of each step in more detail.

## 2.1 Computation of relative sea-level changes

~~In this section we first present the used models to compute relative sea-level changes, and then provide more information about the different relative sea-level configurations that we use for our analysis.~~

### 2.1.1 Coupled ice-sheet – GIA model framework

195 We simulate RSL changes using the coupled ice sheet – GIA model framework PISM-VILMA as described in ~~Albrecht et al. (2023, in prep.)~~ ~~Albrecht et al. (2023, accepted)~~. The Parallel Ice Sheet Model (PISM; <https://www.pism.io>; Bueler and Brown, 2009; Winkelmann et al., 2011), an open-source model which simulates ice sheets and ice shelves, is used to compute the transient evolution of the Antarctic Ice Sheet under external climatic ~~boundary forcings~~ ~~forcing~~. It is interactively coupled to the VIscoelastic Lithosphere and MAntle model (VILMA; Kleemann et al., 2008; Martinec et al., 2018), which calculates the solid Earth and sea-level response to changes in ice loading based on a 3D Earth structure (Bagge et al., 2021). VILMA solves ~~self-consistently~~ the global sea-level equation ~~self-consistently~~, which yields a sea-level fingerprint in response to the redistribution of water masses between ice sheets and ocean, as well as a result of rotational and gravitational feedbacks. ~~The simulations use a coupling interval of 100 years to update changes of ice load and bed topography between PISM and VILMA. For the ice loading While Antarctic Ice Sheet changes are interactively modeled with PISM, ice evolution in the northern hemisphere is prescribed (see more information about this below in Sect. 2.1.2). PISM uses a regular Cartesian grid, with either 16 km (*LGM15k*) or 8 km~~

(yr2300) horizontal resolution. VILMA utilizes a Gauss-Legendre grid and our setup uses the n128 resolution ( $256 \times 512$  grid points) for viscoelastic deformation, while solving the sea level equation on higher resolution (n512,  $1024 \times 2048$  grid points). We use the '3D ref' Earth rheology from Albrecht et al. (2023, accepted), which is equivalent to the 'v\_0.4\_s16' configuration in Bagge et al. (2021). A visualisation of the vertical and lateral viscosity structure in Antarctica as well as the lithosphere thickness is provided in Fig. 5 in Albrecht et al. (2023, accepted). VILMA is initialized with the global present-day ETOPO1 bed topography (Amante and Eakins, 2009; NOAA National Geophysical Data Center, 2009), where the Antarctic region has been replaced with the Bedmap2 dataset (Fretwell et al., 2013). Further information about the PISM-VILMA coupling framework is provided in Albrecht et al. (2023, accepted).

In order to represent the GIA response in the ice sheet domain, we first calculate the change in relative sea level  $\Delta r(c)$  with respect to present-day RSL  $r_{pd} = r(\text{present-day})$ , where  $r(c)$  denotes the new RSL configuration  $c$  computed by PISM-VILMA (see Eq. 1). Subsequently, the present-day ice sheet bedrock topography  $t_{pd}$  is corrected with the shift of relative sea-level change to compute the updated bedrock  $t(c)$ , see Eq. 2.

$$\Delta r(c) = r(c) - r_{pd} \quad (1)$$

$$t(c) = t_{pd} - \Delta r(c) \quad (2)$$

We use the BedMachine Antarctica (v3) dataset (Morlighem, 2022; Morlighem et al., 2020) in original resolution (500 m) for present-day topography and regrid RSL changes  $\Delta r(c)$  from the VILMA to BedMachine grid bilinearly.

### 2.1.2 Relative Sea-Level Configurations

The *LGM15k* configuration represents the difference in relative sea level 15 thousand years before present (kyr BP). It is extracted as a single time slice from a transient coupled ice sheet–GIA simulation over the last 246 kyr BP (representing the last two glacial cycles) described in Albrecht et al. (2023, accepted). The Antarctic Ice Sheet is modeled interactively with PISM, while the ice load history of the northern hemisphere ~~over the last glacial cycle we use the~~ is prescribed by the ICE-6G\_C reconstruction (Stuhne and Peltier, 2015). ~~A detailed description of the coupled PISM-VILMA framework and sensitivities to coupling parameter, resolution and Earth structures is given in Albrecht et al. (2023, in prep.)~~ The Antarctic climate forcing is scaled with temperature anomalies from ice-core reconstructions (Albrecht et al., 2020a). The whole simulation period has been iterated six times to invert for the initial topography, by considering the offset of the present-day modeled topography at the end of the previous run. The coupling interval between ice and GIA models is 100 years and PISM uses a 16 km horizontal resolution.

~~We interpret the computed~~ During the coupled simulation, the maximum AIS extent during the last glacial period is reached at around 15 kyr BP, which is approx. 11 thousand years later than in the northern hemisphere (26 kyr BP, see Fig. S3). This delay agrees well with Clark et al. (2009), suggesting a West Antarctic LGM delay of 4.5–12 kyr with respect to the global LGM sea-level ~~changes relative to the geoid as negative shifts in bathymetry and update the present-day topography of~~

lowstand and the **BedMachine Antarctica (v3) dataset (Morlighem, 2022; Morlighem et al., 2020)**, conservatively regressed to ICE-6G\_C reconstruction. In our simulation, GMSL was approx. 93 m lower than today during that period.

The *icefree* RSL configuration is derived from the long-term solid Earth response to an instant removal of all present-day ice load. Continental ice masses are redistributed as liquid water and added to the ocean mass, which leads to a GMSL rise of approx. 70 m in our simulation. As no dynamic ice-sheet changes are computed, this RSL configuration is computed with a VILMA standalone configuration. The simulation period spans 86 kyr into the future. The long simulation time has been chosen such that the full solid Earth response can unfold (before a possible next ice age), also in regions featuring high mantle viscosities as well as a thick lithosphere and therefore rather long response time scales.

The *yr2300* RSL configuration is derived from a coupled PISM-VILMA simulation using an upper-limit climate forcing. The initial state for PISM is derived as in Reese et al. (2023), with a 400 kyr thermal spinup (using a 16 km horizontal resolution), followed by a 25 kyr full-physics spinup (8 km resolution). First, the historic period (1850–2015) is computed with pre-industrial climate forcing as described in Reese et al. (2023). The climate forcing for the subsequent model period (2015–2300) follows the ISMIP6 2300 extension protocol using a SSP5-8.5 realisation of CESM2 (AE04). The ISMIP6 2300 extension author 245 . We use the best scoring PISM ensemble member (AIS1) from Reese et al. (2023), which uses the following PISM parameters: till effective overburden fraction  $\delta = 1.75\%$  and till water content decay rate  $C_d = 10 \text{ mm a}^{-1}$ . The coupling time step between PISM and VILMA is set to 1 year and PISM uses a 8 km horizontal resolution, ~~for all scenarios accordingly~~. The historic period shows plausible RSL change rates (see Fig. S4), which are comparable to GNSS measurements (Buchta et al., 2022; Scheinert et al., 250 . While the climate forcing reflects an upper end estimate, the dynamic ice-sheet response does not include structural uncertainties of ice-sheet behaviour such as the Marine Ice Cliff Instability (MICI), which can potentially increase Antarctic ice loss by a factor up to 4 but is poorly constrained (IPCC AR6 WG1 Ch. 9.6.3.5, Fox-Kemper et al., 2021). To also include non-Antarctic cryospheric changes and reflect redistributions in the global water budget, we add a uniform GMSL contribution of 3.68 m on the relative sea-level changes computed by PISM-VILMA in a post-processing step (after the coupled simulation has been finished), which is composed from upper end (83th percentile) IPCC estimates for the year 2300 under SSP5-8.5 forcing: the 255 contributions are 1.75 m from the Greenland Ice Sheet, 0.32 m from glaciers, 0.10 m from land-water storage and 1.51 m from thermal expansion (IPCC AR6 WG1 Ch. 9.6.3.5, Fox-Kemper et al., 2021, Table 9.11). By adding a uniform, global mean sea-level offset to relative sea-level changes computed by PISM-VILMA we make the assumption, that regional variations from the global mean around Antarctica, e.g. induced by gravitational or rotational effects in response to these contributions (with origin mostly on the northern hemisphere), are small and not relevant on the scale of our assessment, which uses a vertical 260 resolution of 1 meter to identify access depths from topography.

## 2.2 Identification of critical access depths

### 2.2 Identification of access depths

In order to evaluate how the altered bathymetry ~~changes the water masses that have access onto the continental shelf and into ice-shelf cavities~~ <sup>t(c)</sup> modifies the access of offshore water masses to the ice-sheet grounding lines, we make use of the approach

270 developed in Nicola et al. (2023b, subm.)~~a related study by Nicola et al. (2023b, in discus.)~~. Therein, *oceanic gateways* are defined as the deepest possible ~~entry point~~ *topographic connection* of open ocean water to the grounding lines of the Antarctic Ice Sheet. ~~First, we compute *access depth* maps, which indicate for every location on the continental shelf, the deepest possible topographic~~ This methodology is based on the assumption that inflowing water masses from beyond the continental-shelf break always follows these deepest bathymetric pathways onto the continental shelf and eventually into the ice-shelf cavities.  
 275 Over-deepend regions on the continental shelf are thereby shielded by shallower topography that inhibits the inflow of water masses below the deepest connection to the open ocean. ~~This is implemented with a successive flood-fill algorithm, which starts in the Southern Ocean, far from the continental-shelf break and iteratively propagates to all adjacent grid points that have the same or lower bathymetry. We perform this analysis on 8 horizontal bathymetry resolution and iterate vertically in steps of 1.~~ Then, we evaluate the resulting 2-dimensional field. We systematically analyse the topographic connectedness by calculating  
 280 an access depth map  $d_m(c)$ . This map contains for every grid point on the continental shelf the largest possible depth, for which there is a horizontal oceanic connection to the open ocean (which is defined as  $t > 3700$  m depth) that is not obstructed by bathymetry. We obtain the map of access depths at the present-day grounding-line position for all scenarios. This results in ‘critical access depth’ scalars  $d_c(s, b, g)$ , which indicates the lowest possible connection between the open ocean and the deepest grounding-line fraction  $g$ , ranging from 10  $d_m(c)$  via a ‘Connected Component Analysis’ (CCA), using the implementation by Khrulev (2024). The algorithm iterates the vertical water column from 0 m to 3700 m depth in vertical resolution of 1 m and finds isolated regions that can not be reached from locations classified as open ocean, as they are shielded by shallower topography. A pseudo-code version of the used algorithm is attached in Appendix A. Due to the efficient implementation, an access depth map on 500 to 90°, varied in steps of 5 m resolution can be computed in less than 10 minutes. We calculate critical access depths for each of the scenarios  $s$  described above and for each of the 19 basins  $b$  as defined in Zwally et al. (2012),  
 290 with some of access depth maps  $d_m(c)$  for each topography map  $t(c)$  including the present-day topography  $t_{pd}$ . Supplement Figure S5 shows the difference between bathymetry  $t(c)$  and the basins being merged as in Reese et al. (2018) computed access depth maps  $d_m(c)$ , which visualises the location and magnitude by which deeper parts on the continental shelf are shielded by further offshore, more shallow, topography. The influence of RSL changes  $\Delta r(c)$  on access depth maps can be analysed by the anomaly to present-day access depth map (Eq. 3).  
 295

The deepest lying grounding line sectors typically feature high ice velocities, and thereby the biggest ice fluxes across the

$$\Delta d_m(c) = d_m(c) - d_m(\text{present-day}) \quad (3)$$

From the inferred 2-dimensional access depth maps, we select only the grid cells coinciding with the grounding line mask for further analysis. The grounding line, ~~see also Nicola et al. (2023b, subm.)~~. However, it is difficult to define a uniform threshold of relevant grounding line coverage, where a change in critical access depth is most relevant, due to the great heterogeneity between the basins. We therefore assess changes in critical access depths across the full spectrum between 10% and 90%. ~~mask~~ is defined as all floating ice grid cells, which have a direct neighbouring cell with grounded ice belonging to the main Antarctic continent, which means that islands and ice rises are not considered here.  
 300

We evaluate the sparse access depth map at the grounding line for different basins  $b$  and define the deepest access depth per basin as  $d_{\text{GL},0}(b,c)$ . Furthermore, we calculate access depths with the constraint that at least a certain fraction of the 305 grounding line needs to be reached by this depth:  $d_{\text{GL},g}(b,c)$  is the deepest possible access depth for RSL configuration  $c$ , such that at least  $g\%$  of the grounding line cells in basin  $b$  have a deeper or similar access depth. Using a range of grounding line fractions for  $g \in \{10, 20, \dots, 90\}$ , we thereby obtain values of  $d_{\text{GL},10}(b,c), d_{\text{GL},20}(b,c), \dots, d_{\text{GL},90}(b,c)$  for each basin  $b$  and RSL configuration  $c$ . We use a classification of the AIS and the surrounding ocean into 19 basins as presented in Nicola et al. (in discus., 2023b), which are originally based on AIS drainage basins defined in Zwally et al. (2012), extended 310 and modified by Reese et al. (2018) and adapted by Nicola et al. (in discus. 2023b) to match oceanic gateway pathways for present-day (basin boundaries shown in Fig. 2c). Changes in grounding line access depths to the present-day baseline are computed as in Eq. 4 and 5:

$$\Delta d_{\text{GL},0}(b,c) = d_{\text{GL},0}(b,c) - d_{\text{GL},0}(b, \text{present-day}), \quad (4)$$

$$\Delta d_{\text{GL},g}(b,c) = d_{\text{GL},g}(b,c) - d_{\text{GL},g}(b, \text{present-day}). \quad (5)$$

### 315 2.3 Calculation of marginal ocean properties

We assume that a shift in critical access depths gives water masses from varying depths potential access. The underlying assumption of our methodology is that changes in the grounding line access depth  $d_{\text{GL},0}$  modifies the vertical entry point of water masses that flow onto the continental shelf and to the grounding lines. In order to assess the induced changes, we evaluate the from further offshore and thereby affect the potential melting inside the ice-shelf cavities. We calculate this 320 change in ocean properties by evaluating the vertical column of ocean temperature ( $T_{\text{csb}}$ ) and salinity ( $S_{\text{csb}}$ ) present-day ocean observations at the continental-shelf break for different access depths:  $T_{\text{CSB,mean}}$  is defined as the mean of ocean temperature  $T$  at the continental-shelf break (horizontal position where topography follows  $z = -1800 \text{ m}$  isobath), at the depth of the deepest grounding line access depth  $d_{\text{GL},0}$  (see Eq. 6).

$$T_{\text{CSB,mean}}(b,c) = \text{mean} \{ T(x,y,z) | (x,y) \in \text{CSB}(b) \text{ and } z = d_{\text{GL},0}(b,c) \} \quad (6)$$

325 We define the mean continental-shelf temperature  $\overline{T}_{\text{csb}}(s,b,g)$  as the horizontal average of  $T_{\text{csb}}$  break mask as all grid cells that are in the range of 40 km distance of the 1800 m isobath of present-day bathymetry. CSB( $b$ ) denotes the subset of the continental-shelf break mask in basin  $b$  at critical access depth  $d_c(s,b,g)$ , similar to Nicola et al. (2023b, subm.). We then use the difference  $\Delta \overline{T}_{\text{csb}}(s,b,g)$ . From the computed continental-shelf break temperatures for different RSL configurations  $c$ , we calculate the temperature anomaly with respect to the present-day control conditions for each scenario (see configuration 330 Eq. ??) to modify the ocean forcing input 7) and add them to baseline values used for calculating basal melt rate changes within the ice-sheet model, as described in the next section rates in ice-shelf cavities (see Sec. 2.4 and 2.5 below). Note that the anomaly method diverges from Nicola et al. (2023b, in discus.; revised manuscript), who calculate ocean anomalies between

the continental-shelf break and the calving front location, in order to estimate the present-day basal melt increase due to extensive inflow of warmer offshore water masses into ice-shelf cavities.

335  $\Delta\overline{T}_{\text{csb}}(s, b, g) = \overline{T}_{\text{csb}}(s, b, g) - \overline{T}_{\text{csb}}(s = \text{present-day}, b, g)$

$\Delta T_{\text{CSB, mean}}(b, c) = T_{\text{CSB, mean}}(b, c) - T_{\text{CSB, mean}}(b, \text{present-day})$  (7)

Salinity anomalies  $\Delta\overline{S}_{\text{csb}}(s, b, g)$  values at the continental-shelf break  $S_{\text{CSB, mean}}$  and their anomalies to present-day  $\Delta S_{\text{CSB, mean}}$  are computed accordingly. As in Nicola et al. (2023b, subm.), we use to Eq. 6 and 7. Similar to Nicola et al. (2023b, in discuss.), we make use of the ISMIP6 climatology dataset (Jourdain et al., 2020), which contains potential temperature and practical salinity data points averaged over the period 1995–2017, available 1995–2017 at a 8 km  $\times$  8 km horizontal and 60 m vertical resolution. The dataset is a combination of different data sources like the World Ocean Atlas 2018 (Locarnini et al., 2018; Zweng et al., 2019), the Met Office EN4 subsurface ocean profiles (Good et al., 2013) and the Marine Mammals Exploring Oceans from Pole to Pole (MEOP) dataset (Roquet et al., 2013, 2014; Treasure et al., 2017). Jourdain et al. (2020) merged and extrapolated these data products using a similar method as our CCA approach, which makes their data very suitable for our analysis as missing data has been filled with appropriate values. To acquire ocean properties between discrete vertical data layers, we utilize linear interpolation along the vertical axis.

## 2.4 Computation of basal melt in ice-shelf cavities

For computing basal melt rates we use the Potsdam Ice shelf Cavity mOdule (PICO) as implemented in the ice-sheet model 350 PISM (Reese et al., 2018). PICO parameterizes the vertical overturning circulation in ice-shelf cavities driven by melt-induced buoyancy fluxes, extending the box model by Olbers and Hellmer (2010) to two horizontal dimensions. The module takes ocean temperature and salinity at continental shelf depth from the floor of the continental shelf area as input, typically averaged horizontally per basin, representing the water masses that reach the grounding line. Due to mixing with more buoyant melt water these water masses rise along the ice-shelf base via the ice-pump mechanism (Lewis and Perkin, 1986).

355 As a baseline, we use PICO parameters from Reese et al. (2023, AIS1) including their ocean forcing data, which is based on Schmidtko et al. (2014). The parameters are  $C$ . We compute basal melt rate changes in a pure diagnostic manner without any transient ice sheet changes (except for one special case, explained in Sec. 2.5). Thus, the computed melt rates are solely dependent on the used PICO parameters, the ocean forcing and the ice-sheet geometry. We compare 'baseline' basal melt rates to ones that are obtained by adding RSL derived ocean anomalies ( $\Delta T_{\text{CSB, mean}}, \Delta S_{\text{CSB, mean}}$ ) to the baseline ocean forcing. 360 Depending on the set of experiments, we use different ice-sheet geometries and resolution (further information given below in Section 3.0.2.5).

PICO features two main (circum-Antarctic) parameters to adjust the amount of melting in the ice-shelf cavities: the vertical overturning circulation strength  $C$  (in  $\text{Sv m}^3 \text{kg}^{-1}$  for the strength of the vertical overturning circulation and the heat exchange

365 ), and the heat-exchange coefficient  $\gamma_T^* = 7 \times 10^{-5}$  (in  $10^{-5} \text{ m s}^{-1}$ ). The tuning of Reese et al. (2023) optimises for the best fit of present-day observed melt rates as well as). Reese et al. (2023) tune these two parameters in order to represent realistic melt-rate sensitivities to for given thermal forcing. For each scenario  $s$  and grounding line accessibility  $g$ , we then compute adjusted sub-shelf melt rates  $\bar{m}(s, b, g)$  by adding the computed ocean forcing anomalies  $\Delta T_{\text{CSB}}(s, b, g)$  and  $\Delta S_{\text{CSB}}(s, b, g)$  to each corresponding basin  $b$  in the baseline forcing. Similar to the approach in Jourdain et al. (2020), they correct the input temperature values during this process, which are originally based on Schmidtko et al. (2014), in order to match present-day melt rate observations from Adusumilli et al. (2020). Which PICO parameters we use is explained in the following section.

370 To initialise PISM, we use ice geometry (thickness) and bedrock topography of BedMachine v3 (Morlighem et al., 2020), regressed to a horizontal resolution of 4

## 2.5 Experiment Design

375 In order to estimate the impact of relative sea-level changes on basal melt rates, we conduct different sets of experiments. They can be classified into the set of *present-day sensitivity* experiments and the *applied scenario* set and are all listed in Table 1.

## 2.6 Scenarios

380 In the *present-day sensitivity* set we calculate the effect of different RSL configurations on basal melt rates using a present-day ice-sheet configuration. We thereby test the sensitivity of the present-day ice sheet to RSL configurations from different (past and future) time slices which include the maximum range of plausible RSL changes. These experiments have no real-world application, but are still useful to derive upper-limit estimates of the maximum possible impact of relative sea level on basal melt rates.

385 The set encompasses the experiments LGM15k\_PDsens\_RSLcorrect, icefree\_PDsens\_RSLcorrect and yr2300\_PDsens\_RSLcorrect, where basal melt rates are compared to the present-day baseline experiment PD\_baseline. We use an updated bedrock topography with the respective RSL configuration (see Eq. 2) to compute access depths  $d_{\text{GL},0}(b, c)$  using the present-day ice sheet mask and grounding line position. Similarly, we compute access depths for PD\_baseline, where no RSL changes are applied. We now add the derived changes in ocean forcing ( $\Delta T_{\text{CSB, mean}}$ ,  $\Delta S_{\text{CSB, mean}}$ , see Eq. If not stated otherwise, we will use 7) to the present-day baseline ocean forcing and compute basal melt rates with a present-day ice-sheet configuration. By comparing these melt rates to the baseline experiment, we acquire changes in ice-shelf basal melting driven by artificial RSL configurations for the term Last Glacial Maximum (LGM) with respect to the Antarctic Ice Sheet in the following.

390 In the *icefree* scenario, the solid Earth response to a removal of all present-day ice load is computed. Continental ice masses are redistributed as liquid water and added to the ocean mass, which leads to a GMSL rise of approx. 70 ice-sheet configuration.

395 To compute basal melt rates with PICO, we use bedrock topography and ice thickness from the BedMachine Antarctica (v3) dataset (Morlighem, 2022; Morlighem et al., 2020) regressed to a horizontal resolution of 4 in our simulation. The simulation period spans 86 km. We use the "best" parameter combination from Reese et al. (2023), which is  $\{C = \text{into the future to account}$

**Table 1. Experiment overview.** A list of the experiments conducted for this study. *RSL config* refers to the used relative sea level configuration to update the bedrock topography ( $c$  in Eq. 1 and 2). *Basal melt resolution* indicates the horizontal resolution of the ice-sheet setup used for computing basal melt rates. *deglac* represents a time series from *LGM15k* to present-day with 500 year time slices (more explanation in Sec. 2.5).

This subsection provides more information about the scenarios used to compute RSL changes with the coupled ice

Name	Experiment set	RSL config.	Ice mask	Ocean forcing	Basal melt resolution
PD_baseline	PD sensitivity	PD	PD	PD	4 km
LGM15k_PDsens_RSLcorrect	PD sensitivity	LGM15k	PD	PD + RSL correct	4 GIA model (step 1). The LGM15k
icefree_PDsens_RSLcorrect	PD sensitivity	icefree	PD	PD + RSL correct	4 km
sheet	yr2300_PDsens_RSLcorrect	yr2300	PD	PD + RSL correct	4 GIA model spinup of two glacia
	LGM15k_apply_baseline	applied scenario	PD	LGM15k	16, which is approx. 11 thousand
	LGM15k_apply_RSLcorrect	applied scenario	LGM15k	LGM15k + RSL correct	16, see Fig. km
	yr2300_apply_baseline	applied scenario	PD	yr2300	8 S1). This delay agrees well with
	yr2300_apply_RSLcorrect	applied scenario	yr2300	yr2300 + RSL correct	8 lower than today during that per
	deglac_apply_baseline	applied scenario	PD	deglac	16 km
	deglac_apply_RSLcorrect	applied scenario	deglac	deglac + RSL correct	16 km

PD = present-day, RSL config. = relative sea-level configuration, RSL correct. = relative sea-level correction

for long-term solid Earth response also in regions with strong Earth structure featuring high mantle viscosities and a thick lithosphere.  $2.0 \text{ Sv m}^3 \text{ kg}^{-1}, \gamma_T^* = 5 \times 10^{-5} \text{ m s}^{-1}$ . The baseline ocean forcing for this set of experiments corresponds to the temperature corrected ocean input in Reese et al. (2023).

400

In the second, *applied scenario* set of experiments, we compute RSL derived basal melt rate changes for ice-sheet configurations that correspond to the used RSL configurations. This experiment set is of more realistic nature than the first one, as it considers the correct ice-sheet geometry and corresponding ocean forcing that matches the used RSL configurations. It can therefore be regarded as an estimate of the RSL influence on basal melt rates in realistic scenarios.

405

For the *LGM15k* and *yr2300* RSL configuration, we first compute access depths and melt rates for a baseline scenario (\* *apply\_baseline*), using the corresponding ice-sheet geometry and ocean forcing. Note that the bedrock topography is not updated in these baseline experiments, so no modifications to the ocean forcing due to RSL corrections apply. This is instead done in the subsequent experiments (\* *apply\_RSLcorrect*); computed access depths  $d_{GL,0}$  differ from the baseline experiments as the bedrock topography has been altered by the associated changes in RSL. Using Eq. 6 and 7, we derive corrections 410 in the ocean forcing. By comparing the computed basal melt rates from the \* *apply\_RSLcorrect* to the \* *apply\_baseline* experiments, we compute the RSL impact on basal melt rates in real-world applications.

415 For the *LGM15k* scenario, we start the coupled ice sheet the PICO parameters  $\{C = -0.8\}$  GIA simulations in year 1850 with a historical spin-up phase, where we observe plausible RSL change rates as observed by GNSS measurements. Then, from present-day onwards, the ice sheet climate forcing follows the ISMIP6 2300 extension protocol using a SSP5-8.5 realisation of CESM2 (AE04, The ISMIP6 2300 extension authors, 2022). We use the best scoring member of ice sheet initialisation ensemble from Reese et al. (2023, AIS1) as setup for the Antarctic Ice Sheet. While the climate forcing reflects an upper end estimate, the dynamic ice sheet response does not include structural uncertainties of ice sheet behaviour such as the Marine Ice Cliff Instability (MICI), which can potentially increase Antarctic ice loss by a multiple (IPCC AR6 WG1 Ch. 9.6.3.5, Fox-Kemper et al., 2020). To include also non-Antarctic cryospheric changes and reflect redistributions in the global water budget, we add a uniform GMSL contribution of  $3.68\text{Sv}$  on the relative sea-level changes computed by PISM-VILMA, which is composed from upper end (83th percentile) IPCC estimates for the year 2300 under SSP5-8.5 forcing: the contributions are  $1.75\text{m}^3$  from the Greenland Ice Sheet,  $0.32\text{kg}^{-1}, \gamma_T^* = 1 \times 10^{-5}\text{ m}$  from glaciers,  $0.10\text{s}^{-1}\}$  are used on a horizontal grid resolution of 16 from land-water storage and  $1.51\text{km}$ , similar to Albrecht et al. (2020a). In the *yr2300* case the "max" parameter set from Reese et al. (2023)  $\{C = \text{from thermal expansion (IPCC AR6 WG1 Ch. 9.6.3.5, Fox-Kemper et al., 2021, Table 9.11). By adding a uniform, global mean sea-level offset to relative sea-level changes computed by } 3.0\text{ Sv m}^3\text{ kg}^{-1}, \gamma_T^* = 7 \times 10^{-5}\text{ m s}^{-1}\}$  is used on a horizontal resolution of 8 km.

420 The *applied scenario* set features an additional experiment named *deglac\_apply\_baseline* and *deglac\_apply\_RSLcorrect*. These are similar to the *LGM15k\_apply\_\** experiments, but encompass a time series for the whole deglaciation time span from 15 kyrBP to present-day in steps of 500 years. We compute the RSL-induced ocean forcing corrections for every time slice 425 using the same methodology as for the *LGM15k* case. We then repeat the coupled PISM-VILMA we make the assumption, that regional variations from the global mean around Antarctica, e. g. induced by gravitational or rotational effects in response to these contributions (with origin mostly on the northern hemisphere), are small and not relevant on the scale of our assessment, which uses a vertical resolution of 1 meter to identify critical access depths from topography simulation for the deglaciation period and apply the ocean forcing corrections as a time-dependent anomaly. These experiments are the only ones in this study, 430 where we calculate basal melt rates with RSL-induced ocean corrections in a transient manner (compared to the pure diagnostic analysis for the other experiments).

### 3 Results

435 In this section we describe the results of our analysis investigating the impact of relative sea-level change on Antarctic ice-shelf basal melt rates. First, we describe RSL changes for the *LGM15k* and *icefree* scenarios from and *yr2300* configurations as modeled by the coupled ice sheet–GIA simulations. The derived changes in critical grounding line access depths are described thereafter, before we assess the impact on ocean temperature and salinity conditions continental-shelf break ocean temperatures, which drive the changes in basal melting. Subsequently, we take a look into policy relevant time scales and present results for the We present basal melt changes for the *yr2300* present-day sensitivity scenario, as well as for the *applied scenario* experiment set.

Variations in the RSL pattern can be ascribed to barystatic, rotational, gravitational, or deformational processes. Hereafter, we will refer to changes in the *far-field*, encompassing those arising from both barystatic effects and all GIA-induced alterations in the northern hemisphere that impact the southern hemisphere. This includes primarily the rotational component and alterations in ocean basin volume due to bedrock deformation linked to changes in ice load. In contrast, we categorize *near-field* effects 450 as RSL changes resulting from GIA processes specific to the Antarctic Ice Sheet, primarily involving gravitational and deformational influences.

Our The *LGM15k* simulation shows a maximum grounding line extent close to the continental-shelf break ice sheet features a well advanced grounding line compared to the present-day location and a thicker ice column in almost all locations and regions (see Fig. S6a). The increased ice thickness (up to +3000 m ~~larger than today~~ especially) is especially prominent 455 in the marine basins, where today's largest ice-shelves are located, the Filchner–Ronne (basin 1) and Ross (basin 12) as well as in large portions of the West Antarctic Ice Sheet (basins 13–16). To a lesser extent ~~this is also the case for the~~, thicker ice is also present in the Antarctic Peninsula (basins 17–19) and at the edges of East Antarctica (see Fig. S2). The interior 460 of the East Antarctic Ice Sheet, however, shows a slight decrease of thickness during *LGM15k* (up to -140 m locally) due to less snowfall with colder surface temperature forcing (Nicola et al., 2023a). The additional ice load continental ice mass in Antarctica contributed with around 15 m to the global mean (~~barystatic~~ *barystatic*) sea-level fall of 93 m at 15 kyr BP (130 m during northern hemisphere LGM around 26 kyr BP).

Variations in the RSL pattern can be ascribed to barystatic, rotational, gravitational, or deformational processes. Hereafter, we will refer to changes in the *far-field*, encompassing those arising from both barystatic effects and all GIA-induced alterations in the northern hemisphere that impact the southern hemisphere. This includes primarily the rotational component and alterations 465 in ocean basin volume due to bedrock deformation linked to changes in ice load. In contrast, we categorize *near-field* effects as RSL changes resulting from GIA processes specific to the Antarctic Ice Sheet, primarily involving gravitational and deformational influences.

The change in The changes in sea level relative to present-day  $\Delta r$  as inferred from our coupled ice sheet–GIA model is shown in Fig. 2 for different scenarios RSL configurations. In the *LGM15k* scenario case (Fig. 2a) the GIA response to 470 greater ice extent overcompensates the far-field sea-level fall in many parts: most of West-Antarctica, the Filchner–Ronne and Ross basins and parts of the Peninsula show a total RSL increase, which can ~~mount to + be more than~~ 400 m locally. This is also a consequence of the regionally weak Earth structure due to very low mantle viscosities and a thin lithosphere, which is represented in the 3D Earth structure used as input to by VILMA (Bagge et al., 2021). In contrast, the *LGM15k* far-field sea-level fall dominates the RSL pattern in all regions of East Antarctica. Locally this RSL pattern is dampened through visco- 475 elastic GIA effects, for instance in the Amery (basin 6) or Totten region (basin 8) ~~–, reflected by a reduction of the negative RSL signal in these regions (cf. Fig. 2a)~~. The increased ice load leading to bedrock subsidence also causes a displacement of mantle material into the surrounding areas as part of the forebulge effect, which includes the elastic response of the lithosphere.

This combined process further reduces the relative sea level in those areas ~~and can be observed for example offshore the Filchner-Ronne region (basin 1 and 19), in the Bellingshausen Sea (basin 15) and in the Ross region (basin 12; cf. Fig 2a).~~

480 In the ~~icefree scenario, melting of all ice masses~~ experiment, the transformation of all present-day ice masses into liquid water causes a barystatic sea-level rise of ~~ca.~~ +70 m ~~in our simulations and~~. The VILMA output shows a strong bedrock uplift in all previously glaciated regions in both hemispheres ~~(cf. Fig. 2b)~~. The solid Earth response causes uplift (RSL decrease) of up to 800 m in the interior of the AIS ~~(Fig. 2b)~~. As the ~~the~~ mantle material is drained from the surroundings, ~~bedrock subsidence~~ causing an inverse forebulge effect, ~~such that~~ the RSL increases approx. 20 m more than the far-field sea-level 485 rise in many places of the present-day continental shelf ~~area~~. Areas where the far-field increase in sea level and the near-field bedrock uplift compensate each other (~~zero contour line of RSL change, dashed~~ ~~dashed~~ gray contour line in Fig. 2b) are found close to present-day grounding lines. ~~Results for~~

490 The simulated ice sheet in the yr2300 scenario are presented in ~~Sec.~~ ~~case~~ shows significant grounding line retreat from present-day location, especially in the Filchner-Ronne region (basin 1), the Siple Coast, which is part of the Ross Ice Shelf (basin 12), parts of the Antarctic Peninsula (basins 16, 18, 19) and the West Antarctic basins (no. 13–15). Also in Dronning Maud Land (basins 2–4), Amery (basin 6) and Totten region (basin 8), widespread grounding line retreat can be observed (cf. Fig. ??, S6b). The land ice loss from both northern and southern hemisphere causes a far-field RSL increase in the Southern Ocean around the Antarctic continent mostly in the range of 4–5 m (cf. Fig. 2d). Bedrock uplift caused by grounding line retreat and ice-sheet thinning reduces the depth of the water column, in locally strongly differing magnitudes. In regions of 495 strong uplift, like for instance in the West Antarctic basins, the Antarctic Peninsula, the Filchner–Ronne basin and the Siple Coast, relative sea level shows a net decrease (up to -19 m), overcompensating the far-field sea-level rise. The far-field signal is dominant in large parts of East Antarctica, with some exceptions, like in Dronning Maud Land, the Amery basin or the Totten region.

### 3.2 Changes in critical access depth

#### 500 3.2 Changes in access depths

505 In order to analyse the impact of relative sea-level changes on the access of open ocean water onto the continental shelf, we compute basin-wide critical access depths. We compute the updated topography  $t(c)$  for each RSL configuration  $c$  (Eq. 2) using the changes in relative sea level  $\Delta r$  presented above. Based on this, we compute access depth maps  $d_m(c)$  and retrieve the grounding line access depths  $d_{GL,0}(b, c)$  and  $d_{GL,g}(b, c)$  as explained in ~~Section~~ ~~Sec. 2.2~~ and use bedrock topography, which has been updated with respect to the geoid of the respective scenario presented above. In this section, we explain the relation between  $d_m$  and  $d_{GL,g}$  exemplary for the *present-day sensitivity* experiment set. The *applied scenario* set of experiments uses the same relative sea-level changes  $\Delta r(c)$ , but features different ice masks and thereby grounding line positions. Results from this set are shown further below (Sec. 3.4). Results for  $d_{GL,0}$  are shown in Sec. 3.3 and 3.4.

510 Present-day critical access depths reveal prominent oceanic gateways (Nicola et al., 2023b, subm.) access depths  $d_{GLg}$  (b, present-day) reveal oceanic gateways (Nicola et al., 2023b, in discuss.), e.g. in the Filchner–Ronne basin (no. 1) and the Amery basin (no. 6). This can be inferred from Fig. 3a, where the additional colorbar markers (indicating 30%, 50% and 70%  $g = 30\%, 50\%$  and 70% of grounding-line accessibility, respectively) are placed at same depths (orange bars represent present-day). Here, large parts of the basin these basins are filled with offshore water of the same critical access depth level, due to the retrograde 515 slope with over-deepened bathymetry within the ice-shelf cavity. In the Filchner–Ronne basin more than 75 around 80% of the grounding line is reached by water masses that overflow the topographic sill in 600 595 m depth. In Amery basin this threshold is at 530 526 m depth, reaching ca. 65% of the basin grounding line. We identify oceanic gateways also for example in the Ross (basin 12) and the Amundsen Sea basin (no. 14), where at the deepest open-ocean connection (-570 570 m and -600 575 m, respectively) 30% of present-day grounding lines are directly reached.

520 Figure 3a also shows critical access depths calculated for relative sea-level changes in the above defined scenarios, and how grounding line access depths  $d_{GLg}$  for different RSL configurations of the present-day sensitivity experiments. How they differ from present-day depth (panel b)  $\Delta d_{GLg}$  is presented in Fig. 3b. In the LGM15k scenario configuration, barystatic sea level is about 93 m lower than today, which in first estimate would raise critical access depths make grounding line access depths uniformly shallower in all basins, when only the far-field sea-level change with some distance to the AIS was to be considered. 525 This is indicated by a dotted dashed horizontal line in Fig. 3b. Deviations from this line are caused by regional visco-elastic deformations of the lithosphere and mantle and also by the resulting changes in the gravity potential due to mass redistribution and polar motion, all resulting from changes in ice loading.

530 As the concept of critical access depth relates to the potential access of the grounding line, an estimated shift of critical access depths for given changes in relative sea level is not trivial. It depends on a combination of several factors associated with the horizontal fingerprint of relative sea-level changes, which affects the local bedrock depth and its slope angle. The change of access depths at the grounding line  $\Delta d_{GLg}$  is governed by the combination of different factors like the bedrock topography (retro- or prograde slope), as well as the position and depth of the grounding line, and the horizontal fingerprint of relative sea-level changes. To decipher the response in grounding line access depth changes and understand the deviations to the barystatic far-field signal, it helps to examine the spatial pattern of access depth map changes: Figure 4 shows this exemplarily 535 for the Amundsen Sea region the present-day bedrock topography  $t_{pd}$ , the relative sea-level change  $\Delta r$ , the present-day access depth map  $d_m$  (present-day) and its associated change ( $\Delta d_m$ ) for the LGM15k RSL configuration in the same region, namely the Amundsen Sea Embayment (basin 14) in the LGM15k scenario, where. There, a relatively shallow sill at the front of the continental shelf hinders water masses to reach deeper regions further inland including the present-day grounding line. Relative sea-level change at the outer regions of the continental shelf is dominated by the far-field sea-level change fall, which reduces 540 the sill depth in the LGM15k scenario (meaning the sill is getting shallower). In contrast, relative sea level increases by several hundred meters in the interior of the ice-shelf basin due to increased ice loading and subsidence of the bedrock, counteracting over-compensating the far-field sea-level fall. These two opposed signals of relative sea-level change can also be observed in the schematic of the Filchner Trough are also represented in the introductory schematic (cyan line in Fig. 1(cyan line)). Despite the clear pattern of RSL changes in the Amundsen Sea region (Fig. 4b), the horizontal fingerprint of access-depth changes

545 is very heterogeneous (Fig. 4d): it is generally dominated by the sea-level ~~drop-fall~~ at the sill, ~~while meaning that~~ bedrock subsidence has no additional effect in the over-deepened interior. A ~~lowering-deepening~~ of the access depth only occurs in regions, where present-day topography is higher than the overflow sill (compare Fig. 4a, c and d).

550 In order to determine *critical access depths*, which are defined as one value per basin, the distribution of the horizontally varying *access depths* (see Fig. 4e), in particular at the grounding line, becomes a decisive factor. For comparability we use a grounding line position corresponding to the To derive grounding line access depths  $d_{GLg}$ , we evaluate the spatial access depth map  $d_m$  at the position of the grounding line. Using a present-day ice thickness for all scenarios, which has been horizontally adjusted to obtain the floatation criterion for applied bedrock changes. In the ice-sheet geometry and the RSL configuration *LGM15k* scenario this means for the Amundsen Sea basin that the deepest 45, the deepest 40 % of the grounding line in the Amundsen Sea basin is accessed by shallower ocean water compared to present (up to +8878 m in elevation) as a result of the far-field decrease in sea level. Note that the grounding line in basin 14 has many small patches with higher elevation than the sill at the outer continental shelf, which are not clearly recognisable in Fig. 4d. Shallower parts of the grounding line are instead reached by deeper waters compared to the reference (up to -78204 m) as these regions are subject to bedrock subsidence (see Fig. 4b and 3d). This enhances the “oceanic gateway feature” drastically in the sense that a bigger share of the grounding line is reached at lowest possible *overflow access* depth: in the *LGM15k* case, a vast amount of the entire grounding line 75 % of the grounding line are reached via the deepest grounding line access depth (65497 m) is reached instantly at an overflow depth of -515 m, whereas the lowest deepest connection at present-day is reaching reaches 30 % of the grounding line (at -603575 m; compare blue and orange bars in Fig. 3a, basin 14).

555 Generally, basins that exhibit an overall RSL fall and have negligible bedrock subsidence show shallower critical access depths in the *LGM15k* scenario compared to present day. This is the case for the entire East Antarctic Ice Sheet (basins 2–10) and the Getz basin (no. 13) in West Antarctica (compare Fig. 2a and 3b). The maximum increase in critical access depths is lower. As seen in the Amundsen Sea Embayment, the sign and strength in  $\Delta d_{GLg}$  depends on the fraction of grounding line  $g$  that is considered. Also in other basins we observe a mixed signal in grounding line access depth change for the *LGM15k* RSL configuration, namely in basins 1, 7 and 10–12, with the deepest grounding line access depths getting shallower, while the higher grounding line parts are getting deeper. In most of the East Antarctic basins (2–6, 8, 9)  $\Delta d_{GLg}$  gets shallower for all values of  $g$ . The maximum shallowing is, however, less than the far-field sea-level fall in most cases, because the near-field sea-level effects reduce that sea level fall, when bedrock subsidence dampens the RSL signal locally. In basins where local bedrock subsidence actually exceeds the In the West Antarctic basins 15 and 16, the whole grounding line shows deeper access depths compared to present-day, as the bedrock subsidence over-compensates the far-field sea-level signal, critical access depths can be lower and could allow for deeper water masses reaching the grounding lines. This is the case for Ross basin (no. 12) and Drygalski (no. 11) and most of the rest of the West Antarctic Ice Sheet including the Western Antarctic Peninsula (basin 14–17). Despite strong bedrock subsidence being a necessary factor for deeper critical access depths, it is not necessarily a sufficient one. In the Filehner–Ronne basin (no. 1) the whole grounding line is located in a region where GIA-induced bedrock subsidence overcompensates *LGM15k*’s barystatic sea-level lowstand (sea level fall and no prominent oceanic gateway features exist during present-day in these basins (Nicola et al., 2023b, in discuss.). The presence of even shallower grounding line access

580 depths compared to the far-field sea level fall in basin 12 is explained by the forebulge effect in the respective continental shelf region (cf. Fig. 2a). Nevertheless, critical access depths are uniformly shallower in the *LGM/5k* scenario (for all grounding line percentages, see Fig. 3).

585 Figure 3b), as the RSL signal at the overflow sill in the outer continental-shelf region is dominated by the far-field sea-level fall and Fig. 3 shows grounding line access depths and their changes also for the visco-elastic forebulge effect.

590 **Influence of relative sea-level change on critical access depths in the Totten basin for the *icefree* scenario.** Upper row shows present-day topography (a) and change in relative sea-level in the *icefree* state (b). Lower panels show the derived access depths for present-day bathymetry (c) and the corresponding change in the *icefree* scenario (d). Horizontally adjusted grounding line is shown in orange and the present-day continental shelf area (excluding floating ice) is marked with black contour lines. The zero contour line of RSL changes is marked as a grey dashed line. Magenta borders refer to map extent highlighted in Fig. 2.

595 Also in the *icefree* scenario, bedrock topography is a decisive factor to determine the effect of RSL change on critical access depth. Totten Glacier in East Antarctica, for example (basin and yr2300 RSL configurations of the *present-day sensitivity* experiment set. In the *icefree* case  $\Delta d_{GLg}$  is in the range of  $\pm 115$  m, and thereby in the same order as the far-field barystatic sea-level rise of +70 m. The maximum deepening of grounding line access depths partly exceeds the far-field signal (basins 1, 6, 8), has deeper access depths compared to present day, despite its grounding line being located in a region which is subject to bedrock uplift caused by ice unloading (see Fig. 1 and 12) due to a reverse-forebulge effect, where uplift in the interior of the Antarctic continent leads to draining of mantle material in the vicinity, which causes an increase of the RSL rise.

600 As stated above in Section ??d). As the grounding line depth is much deeper than the overflow sill at the continental-shelf margin, the uplift in the grounding line region has no direct effect on the inferred access depth,  $\Delta r$  is between +5 m and -19 m for the far-field rise in sea level remains the dominating mechanism. In other parts of the basin, east and west of Totten Glacier, where the grounding line depth is at a similar elevation or even higher than the sill depth at the continental-shelf margin, the uplift raises the access depths at the grounding line. This explains the strong decrease of critical access depths for the lowest 10 yr2300 RSL configuration, which is an order of magnitude smaller than the other cases. Due to the scale, most 605 of the changes to present-day are therefore not clearly recognisable in Fig. 3b of the grounding line (-1103b, with two exceptions:  $\Delta d_{GLg}$  is up to -72 m and an increase for the rest (see Fig. 3m in basin 17 and up to -54 m in basin 5. Deviations greater than 20 ??a). The influence of bedrock uplift (at the present-day grounding line position) is important for the Ross sector (basins 11 & 12) and the Bellingshausen Sea (basin 16) and in some basins of East Antarctica (no. 2, 5, 7-10). Many 610 of these basins show competing effects of far-field sea-level rise and bedrock uplift on the estimate of critical access depth. While the deepest parts of the m are found only for high grounding line fractions ( $g \geq 70\%$ ) in the latter case, The validity of basin 17 results is generally questionable, as this basin features only very little grounding line grid cells for the present-day ice-sheet configuration. Note that grounding line access depths in basin 17 are much shallower compared to the other basins (Fig. 3a), which leads to a high gradient of grounding line, below the sill depth, are mostly affected by the far-field sea-level rise, the shallower portions of the grounding line may be influenced by local bedrock uplift and other near-field GIA effects.

615 This explains why in some cases for an increasing percentage of the grounding line reached, changes of critical access depth switch from a deepening to a shallowing signal. For some basins the so-called “forebulge collapse” is important, where in the surrounding of bedrock uplift the drained mantle material causes a reverse signal (increase in RSL), adding to the far-field rise of sea level. This explains critical access depths reducing even more than the far-field signal (e.g. Filehner–Ronne, Amery or Totten basin, see Fig. coverage  $g$  to  $d_{\text{GL,g}}$ . Subsequently, small values in  $\Delta r$  can lead to comparable high  $\Delta d_{\text{GL,g}}$ , 3b).

620 **3.3 Induced changes in ocean properties and sub-shelf melt**

**3.3 Present-day sensitivity experiments**

In general, the thermocline layer is characterised by steep temperature and salinity gradients with depth. The typical vertical profile of ocean potential temperatures at the continental-shelf break shows a strong increase from about  $-1.5^{\circ}\text{C}$  at the surface to about  $0.5^{\circ}\text{C}$  at  $300\text{ m}$  depth (Sec. at the surface to about 0.53.1) and access depth (Sec. at 6003.2) gave a general understanding 625 on how GIA processes influence the connectivity of open-ocean water to ice-sheet grounding lines. In this Section, we carry out the next step of our analysis and analyse how the changes in grounding line access depth influence the water properties (ocean temperature and salinity) that reach the grounding lines, and what changes in basal melting thereby occur. As the functional principal of the PICO model is based on the ice-pump mechanism (Lewis and Perkin, 1986) and takes ocean temperature and salinity at the grounding line as input, which rise upwards along the ice shelf draft (see Sec. depth (2.4), we consider only the 630 deepest grounding line access depth  $d_{\text{GL,0}}$  and its changes in the following.

Figure 5 shows the changes in deepest grounding line access depth  $\Delta d_{\text{GL,0}}$ , the derived modifications in continental-shelf break temperatures  $\Delta T_{\text{csb,mean}}$  and the resulting changes in basal melt rates for the *present-day sensitivity* experiment set (LGM15k\_PDsens\_RSLcorrect, icefree\_PDsens\_RSLcorrect and yr2300\_PDsens\_RSLcorrect). The experiments are compared 635 to the present-day baseline experiment PD\_baseline (see Fig. Sec. S4). Below, it decreases slowly with depth to reach about  $0^{\circ}\text{C}$  at  $1800\text{ m}$  for details). Note that results for basin 11 are not shown as there is no continental shelf region associated with this basin. Absolute basal melt rates are shown in Fig. . Similarly, ocean salinities increase from about 34.0 at the surface to ca. 34.7 at  $600\text{ m}$  depth and stay rather constant below (see Fig. S5–S7 (PD\_baseline) and Fig. Changes in critical access depth within the thermocline layer can be associated with colder and fresher water when moving upwards in the water 640 column, and warmer, saltier water downwards. Temperature and salinity gradients can differ significantly among basins. S8 (\*\_PDsens\_RSLcorrect).

In the *LGM15k* scenario, the implied potential change of present-day temperatures at the For LGM15k\_PDsens\_RSLcorrect access depth changes  $\Delta d_{\text{GL,0}}$  are up to  $125\text{ m}$  shallower due to the applied RSL change (Fig. 5a). Only basin 15 (+3 m) and 17 (+50 m) have deeper access depths. The shallower grounding line access leads to negative continental-shelf break is mostly 645 in the range of  $\pm 0.5^{\circ}\text{C}$  temperatures anomalies in different magnitudes ( $-0.02^{\circ}\text{C}$  with extreme values up to  $\pm 0.7^{\circ}\text{C}$  in basin 2 to  $-0.33^{\circ}\text{C}$ , see in basin 3), which is due to the varying thermocline gradients per basin (cf. Fig. 22b. Maximum changes of salinities are in the range of  $-0.21$  to  $-0.05$  (Fig.  $^{\circ}\text{C}$ ) despite

650 a shallower access depth (-78 ??e). In almost all of East Antarctica and also the eastern part of the Antarctic Peninsula, temperatures and salinities decrease due to the shallower critical access depth (dominated by far-field sea-level fall). This causes a drastic decrease in basal melt rates, mostly of 50m), because the present-day access depth (575 m) is below the thermocline layer, so temperatures increase when moving up the water column from there (cf. Fig. S1). The negative temperature anomalies lead to a reduction in basal melting, which is up to -99 % or more. In the Filchner-Ronne basin (no. 1) and Baudois-Lazarev basin (no. 4) this cooling effect is strong enough to support more refreezing underneath the ice shelves than ice-shelf melting, such that on average, the integrated basal mass flux, becomes negative. In West Antarctica (basins 14–16), in contrast, (basin 655 19) compared to present-day melt rates. Relevant positive changes in basal melt rates increase significantly, up to a doubling of present-day reference values, which is caused by a deepening of critical access depths. In the Ross basin (no. 12) the sign of effective basal melt rate depends on the portion of accessed grounding line. It ranges from a basal melt decrease (max. -35 occur only in basin 14 (+5 %) to an increase (max. and basin 17 (+2010 %) when grounding line coverage of more than 60 is considered. This is due to the previously discussed competing effects of far-field sea-level rise and bedrock uplift, which 660 differs between the different depths of grounding line coverage considered (see See. ??).

665 The *Sensitivity of the icefree scenario* shows a maximum difference of  $\pm 0.5$  RSL configuration to the present-day ice sheet (*icefree\_PDsens\_RSLcorrect*; Fig. 5b) is more heterogeneous across the basins, like indicated in previous results (cf.  $\Delta d_{GLg}$  in continental-shelf break temperatures and a range from  $\pm 0.08$  Sec. in salinities to the present-day reference, but most values are in the range of  $\pm 0.3$  3.2). Access depth changes range from +129 and  $\pm 0.05$  m (deeper) in basin 6 to -72. A reduction in ocean temperatures and salinities occurs where the bedrock uplift is dominant over the far-field sea-level rise, which is most pronounced in basins 7–9 (East Antarctica). As a result, the melt rates reduce significantly from present-day values of 2.6, 7.2 and 2.9 by -81, -75 and -96 at maximum (for basins 7–9, respectively). In other regions, however, where far-field sea-level rise dominates the RSL signal, a rise in local temperatures and salinities results in strong increase of basal melt rate. This is especially the case in some East Antarctic basins (no. 3, 4, 6 and 10), as well as along the Antarctic Peninsula (basins 17–19), 670 where basal melt rates can double or even triple (maximum 3.6-fold increase) compared to present-day values.

675 The *icefree scenario* also shows the important influence of critical access depth with respect to the thermocline depth and vertical gradients: Critical access depth drops by ca. 110 m (at grounding line coverage below 75 shallower) in basin 16. The relationship between access depth change and temperature anomaly follows the same direction for all basins except 10–16, where it is inverse. The same reason as in the *LGM15k* experiment applies here. The maximum derived temperature change at the continental-shelf break due to the RSL corrections ranges from +0.24 in the Filchner-Ronne basin (no. 1), due to the far-field sea-level increase. However, this has basically no effect in temperature and salinity (<0.02 °C (basin 6) to -0.09 °C and <0.01 (basin 13). The derived basal melt rate changes range from more than doubling (+141) as the %) in basin 6 to -26 % in basin 5.

680 Applying the *yr2300* RSL configuration to the present-day critical access depth at approx. -600 ice sheet (*yr2300\_PDsens\_RSLcorrect*, Fig. is located below the transition zone, where temperatures and salinities show much lesser gradients with depth (see Fig. 5c) results in mostly deeper access depths (up to 41 and Fig. S4). In other basins, small changes in critical access depths can induce rather large changes in temperature and melt, when the thermocline gradient at access depth is strong: in the Getz basin

(no.13) a decrease of critical access depths by ~~-22~~ m causes an increase of ocean temperature forcing of ~~0.23~~ and temperature anomalies between ~~-0.001~~ °C which results in an increase of basal melt rate by ~~72~~ (basin 10) and ~~+0.012~~ (for ~~-80~~ °C (basin 6), which would change present-day melt rates up to 6 % grounding line coverage). at maximum.

### 3.4 Applied scenario experiments

#### 3.5 Impact in yr2300 scenario

In order to assess the impact of ~~Testing the sensitivity of a present-day ice-sheet with end-member RSL configurations is useful for an upper-bound estimate of the relative sea-level changes on sub-shelf melt rates also on centennial time scales, we have included a scenario in the analysis, which reflects an upper limit climate forcing scenario until the year 2300. change impact on basal melting, but changes possibly deviate for different ice-sheet configurations. This Section shows the results for RSL-induced basal melt rate changes using the respective ice-sheet configuration from where the RLS configurations *LGM15k* and *yr2300* have been derived from. The *icefree* RSL configuration is not included as in this scenario there is no ice sheet to compute basal melt rate changes for.~~

The far-field RSL increase in the Southern Ocean around the Antarctic continent is mostly in the range of ~~4–5~~ Grounding line access depths  $d_{GL,0}$  are ~~40–153~~ m in the *yr2300* scenario deeper in the *LGM15k\_apply\_RSLcorrect* experiment compared to *LGM15k\_apply\_baseline* (Fig. 2d). Bedrock uplift caused by grounding line retreat and ice sheet thinning reduces the depth of the water column, in locally strongly differing magnitudes. In regions of strong uplift like in the ~~6a~~, resulting in continental-shelf break temperature changes between ~~-0.55~~ °C and ~~+0.10~~ °C. Note that Supplement Figures S1 and S2 show the dependence of temperature and salinity values to their respective grounding line access depths for the baseline and 'RSLcorrect' experiment. The ocean forcing temperatures in *LGM15k\_apply\_baseline* are generally cold enough to suppress any relevant basal melting during the LGM except in the West Antarctic basins (no. 13–15), the ~~including the Western~~ Antarctic Peninsula (no. 16–19), basins 13–17; cf. Fig S7b). Therefore, these are the only basins, where a change in basal mass flux can be observed when applying the RSL derived temperature correction  $\Delta T_{csb,mean}$  to the Filehner–Ronne basin (no. 1) and the Siple Coast in the Ross basin (no. 12), relative sea level is lowered by up to ~~-19~~ baseline forcing. The resulting basal mass flux changes range from ~~-12~~ to ~~+40~~, overcompensating the far-field sea-level rise. The far-field signal is dominant in large parts of East Antarctica, with some exceptions, like in Dronning Maud Land (basins 2–4), the Amery basin (no. 6) or the Totten glacier (basin 8) Gt/year, which relates to relative changes of ~~-15~~ % (basin 17) and ~~+41~~ % (basin 15) compared to the baseline.

We expect shallower critical access depths compared to ~~In order to test whether the RSL correction changes the transient evolution of the Antarctic Ice Sheet during deglaciation, we calculate in the present-day reference mostly in the West Antarctic basins (no. 14–16), with a maximum depth increase of ~~+11~~ deglac\_apply\_RSLcorrect experiment the temperature correction  $T_{csb,mean}$  of *LGM15\_apply\_RSLcorrect* for every 500 years since 15 in these basins, which correspond to a decrease in temperature up to ~~-0.07~~ °C and ~~-0.02~~ kyr BP and apply it as temperature correction to the transient ice-sheet forcing in the~~

coupled PISM-VILMA simulation. Figure in salinity. In East Antarctica, where the increase in far-field 7 shows the transient sea-level rise dominates, critical access depths decrease mostly up to 4 equivalent AIS volume with and without our temperature correction applied. After ca. 2, which leads to an increase of marginal ocean temperatures and salinities of up to +0.03 kyr into the deglaciation run, the RSL temperature correction effect leads to a small delay of ice loss compared to the baseline run (deglac\_apply\_baseline). Within the last 5 and +0.009 kyr of the run, ice loss is slightly faster with the RSL correction applied. The difference at present-day is around 0.4, respectively. Shallower critical access depths for upper grounding line percentages ( $\geq 80$  m Sea Level Equivalent (m SLE), which is relatively small compared to the modeled difference of 14), as found in basins 5–7, are artefacts, which are further explained in the discussion below (Seet m SLE between LGM and present-day and the difference of different VILMA rheology parameters (cf. Fig. 7b in Albrecht et al., 2023, accepted). The RSL correction causes 720 positive as well as negative temperature anomalies, depending on the basin and model time. Access depths and corresponding continental-shelf temperatures as well as PICO input temperatures are shown for different basins and the deglaciation time span in Fig 4). While the bedrock uplift in Dronning Maud Land (basins 2–4) is reflected in a shallowing of critical access depths and an associated decrease of basal melt for higher grounding line coverage ( $\geq 40$ ), this is not observed in Totten basin 725 (no. 8), which also shows an overall RSL reduction locally. In general, the applied RSL correction is substantially smaller than the climate-induced variation in PICO forcing over time, which explains the little effect of relative sea level on the AIS 730 evolution throughout the deglaciation simulation.

Sea-level induced changes on mean melt rates for East Antarctica increase by up to 20. The applied yr2300 experiment (yr2300\_apply\_RSLcorrect) provides comparable results to yr2300\_PDsens\_RSLcorrect: changes in grounding line access depths are in the range of  $\pm 5$  m, which results in a comparable change in continental-shelf break temperature anomalies 735 ( $\leq \pm 0.012^\circ\text{C}$ ). Absolute changes in basal mass flux that results from this RSL adjustment are less than 1.5 compared to present, while they decrease by up to 10 Gt/year. Compared to yr2300\_PDsens\_baseline, these changes are less than 0.4 % in most of West Antarctica (except for basin 13, Getz). This is a relevant but much smaller effect than the changes induced by 740 climate change as expected in the upcoming centuries, e. g. with an average increase of basal mass balance by +450 projected until, which is smaller as in the present-day sensitivity experiment, as climate forcing and basal melting in the 2300 by Greve et al. (2023), or the 13-fold increase of mean basal melt rate in Mathiot and Jourdain (2023, in discuss.) projection are substantially higher (cf. Fig. S7a and c).

## 4 Discussion

In this section we will critically review the methods we used to derive our results, discuss possible limitations and give context to the results. Some important points have already been addressed in Nicola et al. (2023b, subm.) Nicola et al. (2023b, in discuss.) 745, as the dependence of the results on the sub-shelf melt parameterisation (Burgard et al., 2022), the chosen melt parameters for the PICO model or the influence of basin boundaries. Below, we explain which processes we have considered as static in our analysis such as ice-sheet geometry, ocean dynamics and geomorphology.

We here have derived our results using a single set of PICO parameters for the *present-day sensitivity* experiment set, which is tuned to represent present-melt rate sensitivities best (see Sec. 2.5; and Reese et al., 2023). In order to test the influence of PICO parameters on our results, we repeat the analysis with an additional set of PICO parameters, representing the maximum sensitivity to present-day melt rate changes, which is  $\{C = 3.0 \text{ Sv m}^3 \text{ kg}^{-1}, \gamma_T^* = 7 \times 10^{-5} \text{ m s}^{-1}\}$  (cf. Reese et al., 2023). Additionally, we test the robustness of our results by deriving the ocean anomalies ( $\Delta T_{\text{csb,mean}}, \Delta S_{\text{csb,mean}}$ ; Eq. 6 and 7) not only as the mean along the continental-shelf break, but also as maximum values ( $\Delta T_{\text{csb,max}}, \Delta S_{\text{csb,max}}$ ). The influence of PICO parameters in the PD baseline experiment is generally little with exceptions in basins 15–17 (cf. Fig. S8). Thereby, the influence of the basin reduce method (mean vs. max) is larger than the influence of chosen PICO parameters, in all basins except 15–17 (cf. Fig S8).

Not that we have focused on temperature changes at the continental-shelf break throughout this manuscript, as they are far more important for the melting response than salinity anomalies: according to the melt rate estimate depending on the equation of state (Eq. 8; Reese et al., 2018), a temperature anomaly of  $0.5 \text{ }^{\circ}\text{C}$  outweighs the melting response of  $0.2 \text{ psu}$  by approximately the factor 40 (cf. Fig. S1 and ~~discuss other important aspects like data resolution and model parameters. S2:~~  $0.5 \text{ }^{\circ}\text{C} / (0.0572 \text{ }^{\circ}\text{C psu}^{-1} \cdot 0.2 \text{ psu}) \approx 43.7$ ).

To estimate sub-shelf melt changes on paleo time scale scenarios, we use ~~present-day ocean observations~~ as the basis for our analysis, despite the ~~AIS surrounding ocean conditions will likely change considerably on these time scales. The dynamics of~~

The relative sea-level configurations used in this study were informed by coupled PISM-VILMA simulations, which account for the three-dimensional structure of the solid Earth, including laterally varying lithosphere thickness and mantle viscosity. Again, we have used only a single set of 3D Earth rheology parameters (named '3D ref' in Albrecht et al. (2023, accepted) and 'v\_0.4\_s16' in Bagge et al. (2021)) for our analysis, which is showing the best fit to global relative sea level records (Bagge et al., 2021) and represents spatially varying parameters between West and East Antarctica (cf. Fig. 5, Albrecht et al., 2023, accepted). However, there is still considerable uncertainty in the parameters space (van Calcar et al., 2023), which has the potential to change the response in grounding line access depth. Albrecht et al. (2023, accepted), for example, show that a thinner lithosphere and low mantle viscosities, as likely dominant in West Antarctica, supports a larger ice-sheet extent (sea-level relevant Antarctic ice volume can be a few meters larger) and much stronger bedrock subsidence (of the order of 100s of meters), when considering large and long-term changes in climate forcing. By comparing three additional rheology parameter sets ('3D ant', '3D trans' and '3D glob'; cf. supplementary material of Albrecht et al., 2023, accepted) we see diverging RSL changes of up to 200 m during LGM, especially in the Filchner-Ronne basin. It cannot be completely ruled out that the VILMA parameters have a non-negligible effect on our results. However, the ~~Southern Ocean, where warm deep waters rise up to intermediate depths, are strongly influenced by local climatic conditions as wind patterns, precipitation and air temperature forcing (Rintoul, 2018)~~. Also the '3D ref' parameter set we used for our results already represents the upper end of tested RSL changes. As systematic testing of the different VILMA parameter sets is out of scope for this study, this remains future work.

The *applied scenario* experiments rely on ice-sheet simulations with prescribed climate forcing. The corresponding *LGM15k* and *deglaciation* experiments make use of a climate-index method to scale external forcing temperatures (ocean and atmosphere)

785 by ice-core reconstructions (Albrecht et al., 2020a). In the yr2300 experiment, climate anomalies from the global climate model CESM2 are used according to the ISMIP6 2300 protocol (The ISMIP6 2300 extension authors, 2022). We compute continental-shelf break ocean anomalies based on the the present-day ISMIP6 dataset by Jourdain et al. (2020) for all experiments and add these to the respective baseline forcing, despite the discrepancy to present-day climate conditions. The underlying assumption, that any climatic changes in the ocean are uniform with depth is often inaccurate and warrants further scrutiny.

790 Our approach of applying access depth derived ocean anomalies from the continental-shelf region directly to the oceanic input at the grounding lines has a number of further limitations. First of all, we fully rely on the ISMIP6 dataset to represent the current ocean state at the continental-shelf break realistically. Despite the fact that this dataset merges different available data sources (argo floats, ship cruises, satellites and marine mammals), in-situ observations at the Antarctic continent margin still remain sparse in temporal and spatial resolution. Furthermore, our approach does solely rely on the vertical ocean profile and does not reflect other mechanisms: for example, if the grounding line access depth is below the thermocline layer, a change in access depth has little effect on the derived ocean anomaly. However, a thicker layer of intruding CDW, which is likely with 795 RSL increase, has the potential to modify basal melting substantially.

800 A general downside of the anomaly approach is that we do not account for any changes of cross-shelf water transport including modification of water masses on the continental shelf. The processes that regulate the transport of warm offshore waters onto the continental shelf and towards grounding lines are inherently complex and governed by many factors: e.g. topographic features, strength and location of ~~sea-ice formation, sea-ice formation, wind patterns, precipitation, ambient air temperature, freshwater input through basal melting or tides; see Thompson et al. (2018) for a detailed review. How oceanic heat supply to AIS margins operates at a variety of spatial and temporal time scales is described in Colleoni et al. (2018). Models that represent these processes in sufficient resolution are currently actively developed and come at huge computational costs (Pelletier et al., 2022). So including changes of marginal ocean properties and~~ and Colleoni et al. (2018) for detailed reviews. Moreover, as mentioned in the introduction, there is evidence that GIA processes themselves control ocean circulation 805 on the continental shelf and offshore (Rugenstein et al., 2014; Wilmes et al., 2017; Tinto et al., 2019), which is not covered by our methodology. According to Thompson et al. (2018), the Antarctic continental shelf can be classified into three distinct types, namely fresh, dense and warm shelf regions, which differ in terms of ocean dynamics and water mass exchange across the continental-shelf break. Fresh shelves are characterised by a strong Antarctic Slope Current with little cross-shelf ~~exchage lies beyond the scope of the study. Instead, we add the RSL induced changes in ocean properties at the water mass exchange.~~ 810 Dense shelves feature moderate exchange with efficient pathways for both import of CDW and export of Dense Shelf Water. Warm shelves typically exhibit a weak frontal structure which allows for high water mass exchange across the continental shelf break and almost uninhibited access of CDW onto the continental shelf (cf. Thompson et al. (2018)). Our anomaly approach is best suited for warm shelf regions, as there is a direct relationship between the continental-shelf break ~~as anomalies to present-day ocean forcing located inside the temperatures and the water masses on the continental shelf that enter the ice-shelf cavities. It is thus possible to differentiate between ocean forcing changes that are due to RSL related geometric shifts and complementary climatic changes of continental shelf ocean properties. Despite the methodology is less suited for dense~~

815

and fresh continental-shelf regions, it is still valuable for deriving upper-bound estimates of basal melt changes, as the actual changes represent an attenuation.

For our analysis, we use

High-resolution ocean modeling can help to study the dependence of ocean processes to RSL changes, that are not captured by our methodology: a change in isopycnal slopes at the continental-shelf break, changes in thermocline gradients, transport of open ocean water masses onto the continental shelf or how ocean circulation inside the ice-shelf cavities is affected. This possibly requires cavity-resolving ocean model domains down to kilometer scale resolution. Additionally, it is required to represent also different time periods with significantly varied climate conditions and ice-sheet configurations, e.g. the Last Glacial Maximum or climate projections for the year 2300. Considering the long simulation run times and extensive computational costs associated with high-resolution ocean modeling (e.g. Pelletier et al., 2022), as well as the challenges in simulating present-day ~~bed topography data from Bedmachine v3, which we conservatively regridded from the native resolution (500) to 8 horizontally~~ Nieola et al. (2023b, subm.), who use the data at original resolution, find considerable higher critical access depths for present-day, especially towards higher grounding line coverages, which is caused by substantial higher grounding line depths in the finer dataset. Nevertheless, we do not assume that the resolution effects the overall results of the study. conditions, e.g. deriving spinup states or initializing newly created water masses during topographic adaptation, this remains a substantial exercise. Nonetheless, we encourage the community to verify our findings with a more realistic representation of ocean dynamics.

In our study, we have ~~also~~ not considered any ~~geomorphologic processes~~ ~~geomorphologic processes~~ so far. We derive ~~critical~~ access depths through analysing the deepest possible topographic connections between the open ocean and Antarctic grounding line positions. The bedrock on the continental shelf is in many places strongly characterised by troughs and sills, which often determine the access to grounding lines. These topographic features have been formed by previous glacial ice streams and can be in the order of hundreds of meters deep. For example, large gateway-like bed structures were eroded during the last glacials, such as the Filchner Trough or Glomar Challenger Basin in the Ross region, see [Nicola et al. \(2023b, subm.\)](#) [Nicola et al. \(2023b, in discus.\)](#). For paleo ice-sheet simulations, the representation of erosion and sediment transport (Damsgaard et al., 2020) can have an additional control on sub-shelf melt estimates, as we have only considered present-day topography in our analysis. However, the horizontal resolution and precise location ~~modelled~~ ~~modeled~~ by sedimentary models is key for correctly representing the effect of changing topographic features and the subsequent impact on ice-shelf basal melt rates.

The RSL changes for the different scenarios were informed by coupled PISM-VILMA simulations, which account for the ~~three-dimensional structure of the Earth~~, including laterally varying lithosphere thickness and mantle viscosity (Albrecht et al., 2023, in ~~–~~). A thinner lithosphere and low mantle viscosities, as likely dominant in West Antarctica (Bagge et al., 2021), supports a larger ice-sheet extent (sea-level relevant Antarctic ice volume can be a few meters larger) and much stronger bedrock subsidence (of the order of 100s of meters). In our analysis of critical access depth, the uncertainty in 3D Earth structure hence mainly affects the grounding line depth, but it can also have a significant influence on the forebulge (order of 10s of meters) and hence on critical access depths.

In our analysis we consider RSL changes from previously performed coupled ice sheet–GIA model simulations with an evolving ice sheet and grounding line geometry in Antarctica. We then compute and compare RSL-induced changes in ice-shelf basal melt rates with respect to present-day melt rates and ocean conditions, while assuming the same **present-day ice sheet configuration** for all scenarios. This assumption is helpful, as the size, geometry and position of ice shelves alone already influences the local patterns and total amount of basal melting, even with fixed oceanic boundary conditions (De Rydt and Naughten, 2023, in *discuss.*). In case of a major relocation of grounding lines, as for instance at the Last Glacial Maximum, with grounded ice sheet extent to the edge of the continental shelf, would induce large changes in critical access depths, even if the effect of sea level change was not considered. This is a consequence of the heterogeneous topography structure across the continental shelf, which affects grounding line depths. And apparently, for an *icefree* scenario, there would be no grounding lines or ice shelves left to compute sub-shelf melt rates from. In order to assess the RSL impact on ice-shelf basal melt rates independently from other processes, we use the same ice sheet geometry for all sea-level scenarios in our assessment.

The grounding line position is determined by the local ice thickness and the relative sea level. For the present-day ice sheet geometry and the different RSL change patterns, we do let the **grounding line position adjust** to associated changes in bedrock topography, as a static re-evaluation of the floatation criterion, while we neglect the ice-dynamical adjustment to this change in boundary conditions. This horizontal grounding line adjustment corrects for inconsistent grounding line elevation after applying changes in RSL, which would bias the derived critical access depths. A re-computation of the floatation criterion tends to mitigate the resultant critical access depth changes by up to  $\pm 100$  m for the *LGM15k* and *icefree* scenarios. This is shown in Fig. S6 by a comparison of critical access depths with and without re-adjusting the horizontal grounding line position. A repeated analysis with the non-adjusted critical access depths shows the same pattern of basal melt changes, but with slightly greater magnitude (see Fig. S7).

The adjustment of the grounding line causes other issues, as for instance additional **noise in the evaluation of critical access depth changes**. In some cases the adjustment leads to small horizontal shifts in the grounding line of only a few grid cells, which changes the total number of grounding line cells in that basin. When the rest of the grounding line remains unchanged, grounding line coverage of a certain segment can change within a few percent, resulting in jumps of critical access depth, even when the same access depth map (no RSL changes) is evaluated. This is the cause of artefacts that we especially observe in the *yr2300* scenario, where the RSL signal is much smaller compared to the *icefree* or *LGM15k* realisation, and also much smaller than the spatial variability in bed elevation within one grid cell distance (see Fig. S6g, basin 3 and 6, where the unrealistic jumps of -35 and +22 occur for example). We expect this noise to be reduced when running the analysis on a finer horizontal resolution. As the horizontal grounding line adjustment is less relevant for small RSL changes, it might be ignored for the *yr2300* scenario. The result of the repeated analysis can be found in the supplementary Fig. S8, which shows a much clearer and de-noised pattern of basal melt rate changes between West (decrease) and East Antarctica (increase) in the range of  $\pm 20$ .

The analysis is conducted for a range of **grounding line coverage** reaching from 10 to 90, which indicates the grounding line fraction reached by a specific critical access depth in each basin. As shown in Nicola et al. (2023b, *subm.*), the deepest

grounding line segments typically correlate with fast flowing ice streams regions. According to the overturning circulation modeled by PICO, which is supplied by near-ground inflowing water into the ice-shelf cavities, ocean property changes at low grounding line coverages (e.g.  $\leq 30$ ) would already have a major influence on the overall basal melt rates. The other ice-shelf regions, away from the fast flowing ice streams, generally exhibit shallower grounding lines, which require higher grounding line coverage values (e.g.  $\geq 70$ ) to be reached. These lateral margins exert a buttressing force and decelerates flow dynamics of upstream grounded ice (Reese et al., 2017). Feldmann et al. (2022) show in an idealised setup with prescribed sub-shelf melt rates that melting at shear margins is more effective than in ice-stream locations. Due to the design of our study, which follows an indirect approach of translating offshore water mass changes to grounding line inflow, the grounding line coverage remains as an unconstrained parameter. In general, the inferred range of critical access depths and melt to grounding line coverage in one basin is smaller than the range among different basins.

Our analysis shows that the influence of RSL on ocean forcing ( $\pm 1$  on paleo time scales) is of comparable magnitude as the influence of several other relevant processes. First, the blocking or modification of warm water masses before reaching ice-sheet grounding lines: the observed difference of ocean temperatures at the continental shelf break and inside the ice-shelf cavities is up to 3 for present-day (Nicola et al., 2023b, subm.). Second, projected changes of ice-shelf ocean forcing: Naughten et al. (2021) show with high-resolution coupled ocean-ice simulations that a switch from a ‘cold’ to a ‘warm’ cavity could happen within the next century under a strong climate warming scenario, which would increase temperature forcing by about 2 in the Filchner-Ronne basin. And third, the range of offshore ocean thermal forcing on glacial time scales: during glacial climates, we assume that ocean temperatures, used as input for PICO, were cooled down at the surface and are hence bounded below by the surface pressure melting point (about  $-1.9$ ), which is 0.2–3.1 below present-day temperature observations in the different basins (Reese et al., 2018, Fig. 2), marking the lower limit of ocean thermal forcing.

From various ice-sheet simulations we know that already 1 of warming can have large impacts on sub-shelf melting and ice-sheet dynamics, in particular close to tipping thresholds. Thus, the interaction of ocean, sea-level and solid Earth processes, in some Antarctic basins, may contribute significantly to enhanced sea-level rise with impacts on future societies.

## 910 5 Conclusions

In our study we evaluate the potential effects of geometric changes in the water column thickness on ice-shelf basal melt, governed by changes in relative sea level. We compare our estimates to similar effects induced by shifts in climatic boundary conditions, associated with altered wind patterns, sea ice and ocean dynamics. Our analysis shows that relative sea-level changes in the order of 100 meters can induce changes of sub-shelf melting in the range of  $\pm 100$  as a consequence of warm 915 Circumpolar Deep Water intrusions onto the continental shelf and into

Our study presents a simplified methodology to test the impact of relative sea-level changes on Antarctic basal melt rates. For a set of relative sea-level configurations, we derive maximum estimates of how ocean access to ice-sheet grounding lines is modified. Based on relative-sea level induced vertical changes in the ocean column, we use ocean anomalies from the continental-shelf break to compute changes in basal melting inside ice-shelf cavities. The relevancy of this process is bound

920 to the time scales of global We use relative sea-level changes and GIA response and fully unfolds over paleo time-scales. We recommend to consider the influence of configurations representing the Last Glacial Maximum, the climate in the year 2300 and a hypothetically ice-free planet as another end-member configuration.

925 Our results indicate that the effect of relative sea-level changes on Antarctic melt rates is of secondary importance, when compared to corresponding climatic changes. This is confirmed by our transient simulation of deglaciation since the Last Glacial Maximum, where we perform coupled ice sheet – GIA modeling with and without relative-sea level induced temperature corrections. Although our methodology has some simplifications, it still remains useful for an approximate estimation. Nevertheless, high-resolution ocean simulations would be valuable to verify our results, in particular to represent the complex continental-shelf processes and their influence on basal melt rates with changes in relative sea level on ocean forcing for millennial-scale simulations of the Antarctic Ice Sheet. In fact, we estimate significant changes in ice-shelf basal melt rates of  $\pm 20$  already 930 within the next three centuries, which could have important implications for projections of Antarctic ice losses and associated contributions to global sea-level rise.

*Code and data availability.* The data and relevant code will be made publicly available on a public data repository i.e. PANGAEA or Zenodo. DOI links to the repositories will be provided upon publication

## Appendix A: Algorithm: Connected Components Analysis

---

### Algorithm A1 Connected Component Analysis as implemented in Khrulev (2024)

---

```
1: max_depth.py:main
2:     load bed topography (bed, mask)
3:     create depth array: invert bed (*-1) and set all grounded values to -1
4:     call max_depth.py:find_max_depth
5:     create max_depth field and initialize with -1
6:     create mask field and initialize with 0
7:     for D in (0,1,2,...,3700)
8:         set mask to 0
9:         call pism_label_components:label(depth, True, D, 3700, mask)
10:            finds all isolated regions (connected components) that have greater depth than D
11:            and can't be reached from deep ocean (>3700m)
12:            marks isolated regions with 1, rest with 0 in mask
13:            call pism_label_components:update_max_depth(depth, mask, D, mask_depth)
14:            sets max_depth = max(max_depth, D) in all areas where depth>D and reachable from deep
15:            ocean according to mask
16:            call max_depth.prepare_output
17:            write max_depth to file
```

---

935 *Author contributions.* RW and TA conceptualized the study, whereas MK, TA and LN developed the detailed study methodology. MK, TA and LN carried out the analysis and TA contributed the PISM-VILMA simulations. RR provided the PISM-PICO setup. RW, RR and LN co-developed the oceanic gateway methodology. MK wrote the manuscript and prepared the figures, with contributions from LN. All authors contributed to the final version with input and suggestions.

Competing interests. The authors declare that they have no competing interests.

940 *Acknowledgements.* This work was supported by the Deutsche Forschungsgemeinschaft (DFG) in the framework of the priority program SPP 1158 "Antarctic Research with comparative investigations in Arctic ice areas" by the following grant: WI 4556/4-1. MK was financially supported by the Potsdam Graduate School. The work of TA and RW has been conducted within the framework of the PalMod project (grant no. FKZ: 01LP1925D, 01LP2305B), supported by the German Federal Ministry of Education and Research (BMBF) as Research for Sustainability initiative (FONA). TA and RW acknowledge support by OCEAN:ICE, which is co-funded by the European Union, Horizon 945 Europe Funding Programme for research and innovation under grant agreement Nr. 101060452 and by UK Research and Innovation. O:I Contribution number 2. LN was supported by the Studienstiftung des Deutschen Volkes (German National Academic Foundation). MK, LN, RR and RW gratefully acknowledge support by the European Union's Horizon 2020 research and innovation programme under Grant Agreement No. 820575 (TiPACCs). RW further acknowledges support by the European Union's Horizon 2020 under Grant Agreement No. 869304 (PROTECT). Development of PISM is supported by NASA grants 20-CRYO2020-0052 and 80NSSC22K0274 and NSF grant 950 OAC-2118285. The authors gratefully acknowledge the European Regional Development Fund (ERDF), the German Federal Ministry of Education and Research and the Land Brandenburg for supporting this project by providing resources on the high performance computer system at the Potsdam Institute for Climate Impact Research.

## References

Adusumilli, S., Fricker, H. A., Medley, B., Padman, L., and Siegfried, M. R.: Interannual variations in meltwater input to the Southern Ocean  
955 from Antarctic ice shelves, *Nature Geoscience*, 13, 616–620, <https://doi.org/10.1038/s41561-020-0616-z>, 2020.

Albrecht, T., Winkelmann, R., and Levermann, A.: Glacial-cycle simulations of the Antarctic Ice Sheet with the Parallel Ice Sheet Model  
(PISM) – Part 1: Boundary conditions and climatic forcing, *The Cryosphere*, 14, 599–632, <https://doi.org/10.5194/tc-14-599-2020>, 2020a.

Albrecht, T., Winkelmann, R., and Levermann, A.: Glacial-cycle simulations of the Antarctic Ice Sheet with the Parallel Ice Sheet Model  
(PISM) – Part 2: Parameter ensemble analysis, *The Cryosphere*, 14, 633–656, <https://doi.org/10.5194/tc-14-633-2020>, 2020b.

960 Albrecht, T., Bagge, M., and Klemann, V.: Feedback mechanisms controlling Antarctic glacial cycle dynamics simulated with a coupled ice  
sheet–solid Earth model, <https://doi.org/10.5194/egusphere-2023-2990>, 2023.

Amante, C. and Eakins, B. W.: ETOPO1 Arc-Minute Global Relief Model: Procedures, Data Sources and Analysis, NOAA Technical  
Memorandum NESDIS NGDC-24, National Geophysical Data Center, NOAA, Boulder, <https://doi.org/10.7289/V5C8276M>, 2009.

965 Bagge, M., Klemann, V., Steinberger, B., Latinović, M., and Thomas, M.: Glacial-Isostatic Adjustment Models Using Geodynamically  
Constrained 3D Earth Structures, *Geochemistry, Geophysics, Geosystems*, 22, <https://doi.org/10.1029/2021gc009853>, 2021.

Barletta, V. R., Bevis, M., Smith, B. E., Wilson, T., Brown, A., Bordoni, A., Willis, M., Khan, S. A., Rovira-Navarro, M., Dalziel, I., Smalley,  
R., Kendrick, E., Konfal, S., Caccamise, D. J., Aster, R. C., Nyblade, A., and Wiens, D. A.: Observed rapid bedrock uplift in Amundsen  
Sea Embayment promotes ice-sheet stability, *Science*, 360, 1335–1339, <https://doi.org/10.1126/science.aa01447>, 2018.

Bentley, M. J., Cofaigh, C. Ó., Anderson, J. B., Conway, H., Davies, B., Graham, A. G., Hillenbrand, C.-D., Hodgson, D. A., Jamieson,  
970 S. S., Larter, R. D., Mackintosh, A., Smith, J. A., Verleyen, E., Ackert, R. P., Bart, P. J., Berg, S., Brunstein, D., Canals, M., Colhoun,  
E. A., Crosta, X., Dickens, W. A., Domack, E., Dowdeswell, J. A., Dunbar, R., Ehrmann, W., Evans, J., Favier, V., Fink, D., Fogwill,  
C. J., Glasser, N. F., Gohl, K., Golledge, N. R., Goodwin, I., Gore, D. B., Greenwood, S. L., Hall, B. L., Hall, K., Hedding, D. W., Hein,  
A. S., Hocking, E. P., Jakobsson, M., Johnson, J. S., Jomelli, V., Jones, R. S., Klages, J. P., Kristoffersen, Y., Kuhn, G., Leventer, A.,  
975 Licht, K., Lilly, K., Lindow, J., Livingstone, S. J., Massé, G., McGlone, M. S., McKay, R. M., Melles, M., Miura, H., Mulvaney, R., Nel,  
W., Nitsche, F. O., O'Brien, P. E., Post, A. L., Roberts, S. J., Saunders, K. M., Selkirk, P. M., Simms, A. R., Spiegel, C., Stolldorf, T. D.,  
Sugden, D. E., van der Putten, N., van Ommen, T., Verfaillie, D., Vyverman, W., Wagner, B., White, D. A., Witus, A. E., and Zwart, D.:  
A community-based geological reconstruction of Antarctic Ice Sheet deglaciation since the Last Glacial Maximum, *Quaternary Science  
Reviews*, 100, 1–9, <https://doi.org/10.1016/j.quascirev.2014.06.025>, 2014.

Buchta, E., Scheinert, M., King, M., Wilson, T., Kendrick, E., Koulali, A., Clarke, P., and Knöfel, C.: GIANT-REGAIN:  
980 A comprehensive analysis of geodetic GNSS recordings in Antarctica for geodetic and geodynamic applications, in: SCAR  
Open Science Conference 2022, p. 347, SCAR, <https://scar.org/~documents/conferences/scar-open-science-conferences/abstracts/scar-open-science-conference-2022-abstracts> (last access: 06 August, 2024), 2022.

Bueler, E. and Brown, J.: Shallow shelf approximation as a “sliding law” in a thermomechanically coupled ice sheet model, *Journal of  
Geophysical Research*, 114, <https://doi.org/10.1029/2008jf001179>, 2009.

985 Burgard, C., Jourdain, N. C., Reese, R., Jenkins, A., and Mathiot, P.: An assessment of basal melt parameterisations for Antarctic ice shelves,  
*The Cryosphere*, 16, 4931–4975, <https://doi.org/10.5194/tc-16-4931-2022>, 2022.

Chandler, D., Langebroek, P., Reese, R., Albrecht, T., Garbe, J., and Winkelmann, R.: Antarctic Ice Sheet tipping in the last 800 kyr warns  
of future ice loss, <https://doi.org/10.21203/rs.3.rs-3042739/v1>, in review, 2023.

Chandler, D. M. and Langebroek, P. M.: Glacial-interglacial Circumpolar Deep Water temperatures during the last 800,000 years: estimates  
990 from a synthesis of bottom water temperature reconstructions, <https://doi.org/10.5194/egusphere-2023-850>, in review, 2023.

Clark, P. U., Dyke, A. S., Shakun, J. D., Carlson, A. E., Clark, J., Wohlfarth, B., Mitrovica, J. X., Hostetler, S. W., and McCabe, A. M.: The  
Last Glacial Maximum, *Science*, 325, 710–714, <https://doi.org/10.1126/science.1172873>, 2009.

Colleoni, F., Santis, L. D., Siddoway, C. S., Bergamasco, A., Golledge, N. R., Lohmann, G., Passchier, S., and Siegert, M. J.: Spatio-temporal  
variability of processes across Antarctic ice-bed–ocean interfaces, *Nature Communications*, 9, <https://doi.org/10.1038/s41467-018-04583-0>, 2018.

Coulon, V., Bulthuis, K., Whitehouse, P. L., Sun, S., Haubner, K., Zipf, L., and Pattyn, F.: Contrasting Response of West and East Antarctic  
Ice Sheets to Glacial Isostatic Adjustment, *Journal of Geophysical Research: Earth Surface*, 126, <https://doi.org/10.1029/2020jf006003>,  
2021.

Damsgaard, A., Goren, L., and Suckale, J.: Water pressure fluctuations control variability in sediment flux and slip dynamics beneath glaciers  
1000 and ice streams, *Communications Earth & Environment*, 1, <https://doi.org/10.1038/s43247-020-00074-7>, 2020.

De Rydt, J. and Naughten, K.: Geometric amplification and suppression of ice-shelf basal melt in West Antarctica,  
<https://doi.org/10.5194/egusphere-2023-1587>, in review, 2023.

Farrell, W. E. and Clark, J. A.: On Postglacial Sea Level, *Geophysical Journal of the Royal Astronomical Society*, 46, 647–667,  
<https://doi.org/10.1111/j.1365-246x.1976.tb01252.x>, 1976.

1005 Feldmann, J., Reese, R., Winkelmann, R., and Levermann, A.: Shear-margin melting causes stronger transient ice discharge than ice-stream  
melting in idealized simulations, *The Cryosphere*, 16, 1927–1940, <https://doi.org/10.5194/tc-16-1927-2022>, 2022.

Fox-Kemper, B., Hewitt, H., Xiao, C., Aðalgeirsdóttir, G., Drijfhout, S., Edwards, T., Golledge, N., Hemer, M., Kopp, R., Krinner, G.,  
Mix, A., Notz, D., Nowicki, S., Nurhati, I., Ruiz, L., Sallée, J.-B., Slangen, A., and Yu, Y.: Ocean, Cryosphere and Sea Level Change,  
in: *Climate Change 2021: The Physical Science Basis. Contribution of Working Group I to the Sixth Assessment Report of the Inter-  
governmental Panel on Climate Change*, edited by Masson-Delmotte, V., Zhai, P., Pirani, A., Connors, S., Péan, C., Berger, S., Caud,  
N., Chen, Y., Goldfarb, L., Gomis, M., Huang, M., Leitzell, K., Lonnoy, E., Matthews, J., Maycock, T., Waterfield, T., Yelekçi, O., Yu,  
R., and Zhou, B., book section 9, p. 1211–1362, Cambridge University Press, Cambridge, United Kingdom and New York, NY, USA,  
<https://doi.org/10.1017/9781009157896.011>, 2021.

1010 Fretwell, P., Pritchard, H. D., Vaughan, D. G., Bamber, J. L., Barrand, N. E., Bell, R., Bianchi, C., Bingham, R. G., Blankenship, D. D.,  
Casassa, G., Catania, G., Callens, D., Conway, H., Cook, A. J., Corr, H. F. J., Damaske, D., Damm, V., Ferraccioli, F., Forsberg, R., Fujita,  
S., Gim, Y., Gogineni, P., Griggs, J. A., Hindmarsh, R. C. A., Holmlund, P., Holt, J. W., Jacobel, R. W., Jenkins, A., Jokat, W., Jordan,  
T., King, E. C., Kohler, J., Krabill, W., Riger-Kusk, M., Langley, K. A., Leitchenkov, G., Leuschen, C., Luyendyk, B. P., Matsuoka, K.,  
Mouginot, J., Nitsche, F. O., Nogi, Y., Nost, O. A., Popov, S. V., Rignot, E., Rippin, D. M., Rivera, A., Roberts, J., Ross, N., Siegert, M. J.,  
Smith, A. M., Steinhage, D., Studinger, M., Sun, B., Tinto, B. K., Welch, B. C., Wilson, D., Young, D. A., Xiangbin, C., and Zirizzotti,  
A.: Bedmap2: improved ice bed, surface and thickness datasets for Antarctica, *The Cryosphere*, 7, 375–393, <https://doi.org/10.5194/tc-7-375-2013>, 2013.

1015 Garbe, J., Albrecht, T., Levermann, A., Donges, J. F., and Winkelmann, R.: The hysteresis of the Antarctic ice sheet, *Nature*, 585, 538–544,  
<https://doi.org/10.1038/s41586-020-2727-5>, 2020.

Gebbie, G.: Cancelation of Deglacial Thermosteric Sea Level Rise by a Barosteric Effect, *Journal of Physical Oceanography*, 50, 3623–3639,  
1020 <https://doi.org/10.1175/jpo-d-20-0173.1>, 2020.

Gomez, N., Latychev, K., and Pollard, D.: A Coupled Ice Sheet–Sea Level Model Incorporating 3D Earth Structure: Variations in Antarctica during the Last Deglacial Retreat, *Journal of Climate*, 31, 4041–4054, <https://doi.org/10.1175/jcli-d-17-0352.1>, 2018.

Gomez, N., Weber, M. E., Clark, P. U., Mitrovica, J. X., and Han, H. K.: Antarctic ice dynamics amplified by Northern Hemisphere sea-level forcing, *Nature*, 587, 600–604, <https://doi.org/10.1038/s41586-020-2916-2>, 2020.

1030 Good, S. A., Martin, M. J., and Rayner, N. A.: EN4: Quality controlled ocean temperature and salinity profiles and monthly objective analyses with uncertainty estimates, *Journal of Geophysical Research: Oceans*, 118, 6704–6716, <https://doi.org/10.1002/2013jc009067>, 2013.

Gregory, J. M., Griffies, S. M., Hughes, C. W., Lowe, J. A., Church, J. A., Fukimori, I., Gomez, N., Kopp, R. E., Landerer, F., Cozannet, G. L., Ponte, R. M., Stammer, D., Tamisiea, M. E., and van de Wal, R. S. W.: Concepts and Terminology for Sea Level: Mean, Variability and Change, Both Local and Global, *Surveys in Geophysics*, 40, 1251–1289, <https://doi.org/10.1007/s10712-019-09525-z>, 2019.

1035 Greve, R., Chambers, C., Obase, T., Saito, F., Chan, W.-L., and Abe-Ouchi, A.: Future projections for the Antarctic ice sheet until the year 2300 with a climate-index method, *Journal of Glaciology*, pp. 1–11, <https://doi.org/10.1017/jog.2023.41>, 2023.

Gulev, S., Thorne, P., Ahn, J., Dentener, F., Domingues, C., Gerland, S., Gong, D., Kaufman, D., Nnamchi, H., Quaas, J., Rivera, J., Sathyendranath, S., Smith, S., Trewin, B., von Schuckmann, K., and Vose, R.: Changing State of the Climate System, in: *Climate Change 2021: The Physical Science Basis. Contribution of Working Group I to the Sixth Assessment Report of the Intergovernmental Panel on Climate Change*, edited by Masson-Delmotte, V., Zhai, P., Pirani, A., Connors, S., Péan, C., Berger, S., Caud, N., Chen, Y., Goldfarb, L., Gomis, M., Huang, M., Leitzell, K., Lonnoy, E., Matthews, J., Maycock, T., Waterfield, T., Yelekçi, O., Yu, R., and Zhou, B., book section 2, p. 287–422, Cambridge University Press, Cambridge, United Kingdom and New York, NY, USA, <https://doi.org/10.1017/9781009157896.004>, 2021.

1040 Hellmer, H. H., Kauker, F., Timmermann, R., Determann, J., and Rae, J.: Twenty-first-century warming of a large Antarctic ice-shelf cavity by a redirected coastal current, *Nature*, 485, 225–228, <https://doi.org/10.1038/nature11064>, 2012.

Horwath, M., Gutknecht, B. D., Cazenave, A., Palanisamy, H. K., Marti, F., Marzeion, B., Paul, F., Bris, R. L., Hogg, A. E., Otosaka, I., Shepherd, A., Döll, P., Cáceres, D., Schmied, H. M., Johannessen, J. A., Nilsen, J. E. Ø., Raj, R. P., Forsberg, R., Sørensen, L. S., Barletta, V. R., Simonsen, S. B., Knudsen, P., Andersen, O. B., Ranndal, H., Rose, S. K., Merchant, C. J., Macintosh, C. R., von Schuckmann, K., Novotny, K., Groh, A., Restano, M., and Benveniste, J.: Global sea-level budget and ocean-mass budget, with a focus on advanced data products and uncertainty characterisation, *Earth System Science Data*, 14, 411–447, <https://doi.org/10.5194/essd-14-411-2022>, 2022.

1045 Jones, R. S., Johnson, J. S., Lin, Y., Mackintosh, A. N., Sefton, J. P., Smith, J. A., Thomas, E. R., and Whitehouse, P. L.: Stability of the Antarctic Ice Sheet during the pre-industrial Holocene, *Nature Reviews Earth & Environment*, 3, 500–515, <https://doi.org/10.1038/s43017-022-00309-5>, 2022.

Jourdain, N. C., Asay-Davis, X., Hattermann, T., Straneo, F., Seroussi, H., Little, C. M., and Nowicki, S.: A protocol for calculating basal melt rates in the ISMIP6 Antarctic ice sheet projections, *The Cryosphere*, 14, 3111–3134, <https://doi.org/10.5194/tc-14-3111-2020>, 2020.

1050 Khrulev, C.: PISM’s connected component labeling implementation, <https://github.com/pism/label-components/>, 2024.

Klemann, V., Martinec, Z., and Ivins, E. R.: Glacial isostasy and plate motion, *Journal of Geodynamics*, 46, 95–103, <https://doi.org/10.1016/j.jog.2008.04.005>, 2008.

Lambeck, K., Rouby, H., Purcell, A., Sun, Y., and Sambridge, M.: Sea level and global ice volumes from the Last Glacial Maximum to the Holocene, *Proceedings of the National Academy of Sciences*, 111, 15 296–15 303, <https://doi.org/10.1073/pnas.1411762111>, 2014.

1060 Lewis, E. L. and Perkin, R. G.: Ice pumps and their rates, *Journal of Geophysical Research: Oceans*, 91, 11 756–11 762, <https://doi.org/10.1029/JC091iC10p11756>, 1986.

Locarnini, M., Mishonov, A., Baranova, O., Boyer, T., Zweng, M., Garcia, H., Reagan, J., Seidov, D., Weathers, K., Paver, C., and Smolyar, I.: World Ocean Atlas 2018, Volume 1: Temperature, Report, [https://data.nodc.noaa.gov/woa/WOA18/DOC/woa18\\_vol1.pdf](https://data.nodc.noaa.gov/woa/WOA18/DOC/woa18_vol1.pdf), 2018.

1065 Marcos, M. and Amores, A.: Quantifying anthropogenic and natural contributions to thermosteric sea level rise: Marcos and Amores: Anthropogenic ocean warming, *Geophysical Research Letters*, 41, 2502–2507, <https://doi.org/10.1002/2014gl059766>, 2014.

Martinec, Z., Kleemann, V., van der Wal, W., Riva, R. E. M., Spada, G., Sun, Y., Melini, D., Kachuck, S. B., Barletta, V., Simon, K., A., G., and James, T. S.: A benchmark study of numerical implementations of the sea level equation in GIA modelling, *Geophysical Journal International*, 215, 389–414, <https://doi.org/10.1093/gji/ggy280>, 2018.

1070 Mathiot, P. and Jourdain, N. C.: High-end projections of Southern Ocean warming and Antarctic ice shelf melting in conditions typical of the end of the 23rd century, <https://doi.org/10.5194/egusphere-2023-1606>, in review, 2023.

Miller, K. G., Browning, J. V., Schmelz, W. J., Kopp, R. E., Mountain, G. S., and Wright, J. D.: Cenozoic sea-level and cryospheric evolution from deep-sea geochemical and continental margin records, *Science advances*, 6, eaaz1346, <https://doi.org/10.1126/sciadv.aaz1346>, 2020.

Mitrovica, J. X., Wahr, J., Matsuyama, I., and Paulson, A.: The rotational stability of an ice-age earth, *Geophysical Journal International*, 1075 161, 491–506, <https://doi.org/10.1111/j.1365-246X.2005.02609.x>, 2005.

Morlighem, M.: MEaSUREs BedMachine Antarctica, Version 3 [dataset], <https://doi.org/10.5067/FPSU0V1MWUB6>, 2022.

Morlighem, M., Rignot, E., Binder, T., Blankenship, D., Drews, R., Eagles, G., Eisen, O., Ferraccioli, F., Forsberg, R., Fretwell, P., Goel, V., Greenbaum, J. S., Gudmundsson, H., Guo, J., Helm, V., Hofstede, C., Howat, I., Humbert, A., Jokat, W., Karlsson, N. B., Lee, W. S., Matsuoka, K., Millan, R., Mouginot, J., Paden, J., Pattyn, F., Roberts, J., Rosier, S., Ruppel, A., Seroussi, H., Smith, E. C., Steinhage, 1080 Sun, B., van den Broeke, M. R., van Ommen, T. D., van Wessem, M., and Young, D. A.: Deep glacial troughs and stabilizing ridges unveiled beneath the margins of the Antarctic ice sheet, *Nature Geoscience*, 13, 132–137, <https://doi.org/10.1038/s41561-019-0510-8>, 2020.

Naughten, K. A., Rydt, J. D., Rosier, S. H. R., Jenkins, A., Holland, P. R., and Ridley, J. K.: Two-timescale response of a large Antarctic ice shelf to climate change, *Nature Communications*, 12, <https://doi.org/10.1038/s41467-021-22259-0>, 2021.

1085 Nicholls, K. W., Østerhus, S., Makinson, K., Gammelsrød, T., and Fahrbach, E.: Ice-ocean processes over the continental shelf of the southern Weddell Sea, Antarctica: A review, *Reviews of Geophysics*, 47, <https://doi.org/10.1029/2007rg000250>, 2009.

Nicola, L., Notz, D., and Winkelmann, R.: Revisiting temperature sensitivity: how does Antarctic precipitation change with temperature?, *The Cryosphere*, 17, 2563–2583, <https://doi.org/10.5194/tc-17-2563-2023>, 2023a.

Nicola, L., Reese, R., Kreuzer, M., Albrecht, T., and Winkelmann, R.: Oceanic gateways to Antarctic grounding lines – Impact of critical 1090 access depths on sub-shelf melt, *EGUphere*, 2023, 1–30, <https://doi.org/10.5194/egusphere-2023-2583>, 2023b.

NOAA National Geophysical Data Center: ETOPO1 1 Arc-Minute Global Relief Model, <https://doi.org/10.7289/V5C8276M>, 2009.

Olbers, D. and Hellmer, H.: A box model of circulation and melting in ice shelf caverns, *Ocean Dynamics*, 60, 141–153, <https://doi.org/10.1007/s10236-009-0252-z>, 2010.

Otosaka, I. N., Shepherd, A., Ivins, E. R., Schlegel, N.-J., Amory, C., van den Broeke, M. R., Horwath, M., Joughin, I., King, M. D., Krinner, 1095 G., Nowicki, S., Payne, A. J., Rignot, E., Scambos, T., Simon, K. M., Smith, B. E., Sørensen, L. S., Velicogna, I., Whitehouse, P. L., A., G., Agosta, C., Ahlstrøm, A. P., Blazquez, A., Colgan, W., Engdahl, M. E., Fettweis, X., Forsberg, R., Gallée, H., Gardner, A., Gilbert, L., Gourmelen, N., Groh, A., Gunter, B. C., Harig, C., Helm, V., Khan, S. A., Kittel, C., Konrad, H., Langen, P. L., Lecavalier, B. S., Liang, C.-C., Loomis, B. D., McMillan, M., Melini, D., Mernild, S. H., Mottram, R., Mouginot, J., Nilsson, J., Noël, B., Pattle, M. E., Peltier, W. R., Pie, N., Roca, M., Sasgen, I., Save, H. V., Seo, K.-W., Scheuchl, B., Schrama, E. J. O., Schröder, L., Simonsen, S. B., Slater, T., Spada, G.,

1100 Sutterley, T. C., Vishwakarma, B. D., van Wessem, J. M., Wiese, D., van der Wal, W., and Wouters, B.: Mass balance of the Greenland and Antarctic ice sheets from 1992 to 2020, *Earth System Science Data*, 15, 1597–1616, <https://doi.org/10.5194/essd-15-1597-2023>, 2023.

Pelletier, C., Fichefet, T., Goosse, H., Haubner, K., Helsen, S., Huot, P.-V., Kittel, C., Klein, F., clec'h, S. L., van Lipzig, N. P. M., Marchi, S., Massonnet, F., Mathiot, P., Moravveji, E., Moreno-Chamarro, E., Ortega, P., Pattyn, F., Souverijns, N., Achter, G. V., Broucke, S. V., Vanhulle, A., Verfaillie, D., and Zipf, L.: PARASO, a circum-Antarctic fully coupled ice-sheet–ocean–sea-ice–atmosphere–land model involving f.ETISh1.7, NEMO3.6, LIM3.6, COSMO5.0 and CLM4.5, *Geoscientific Model Development*, 15, 553–594, <https://doi.org/10.5194/gmd-15-553-2022>, 2022.

Pollard, D., Gomez, N., and Deconto, R. M.: Variations of the Antarctic Ice Sheet in a Coupled Ice Sheet–Earth–Sea Level Model: Sensitivity to Viscoelastic Earth Properties, *Journal of Geophysical Research: Earth Surface*, 122, 2124–2138, <https://doi.org/10.1002/2017jf004371>, 2017.

1110 Pritchard, H. D., Ligtenberg, S. R. M., Fricker, H. A., Vaughan, D. G., van den Broeke, M. R., and Padman, L.: Antarctic ice-sheet loss driven by basal melting of ice shelves, *Nature*, 484, 502–505, <https://doi.org/10.1038/nature10968>, 2012.

Reese, R., Gudmundsson, G. H., Levermann, A., and Winkelmann, R.: The far reach of ice-shelf thinning in Antarctica, *Nature Climate Change*, 8, 53–57, <https://doi.org/10.1038/s41558-017-0020-x>, 2017.

Reese, R., Albrecht, T., Mengel, M., Asay-Davis, X., and Winkelmann, R.: Antarctic sub-shelf melt rates via PICO, *The Cryosphere*, 12, 1115 1969–1985, <https://doi.org/10.5194/tc-12-1969-2018>, 2018.

Reese, R., Garbe, J., Hill, E. A., Urruty, B., Naughten, K. A., Gagliardini, O., Durand, G., Gillet-Chaulet, F., Gudmundsson, G. H., Chandler, D., Langebroek, P. M., and Winkelmann, R.: The stability of present-day Antarctic grounding lines – Part 2: Onset of irreversible retreat of Amundsen Sea glaciers under current climate on centennial timescales cannot be excluded, *The Cryosphere*, 17, 3761–3783, <https://doi.org/10.5194/tc-17-3761-2023>, 2023.

1120 Rignot, E., Mouginot, J., Scheuchl, B., van den Broeke, M., van Wessem, M. J., and Morlighem, M.: Four decades of Antarctic Ice Sheet mass balance from 1979–2017, *Proceedings of the National Academy of Sciences*, 116, 1095–1103, <https://doi.org/10.1073/pnas.1812883116>, 2019.

Rintoul, S. R.: The global influence of localized dynamics in the Southern Ocean, *Nature*, 558, 209–218, <https://doi.org/10.1038/s41586-018-0182-3>, 2018.

1125 Rintoul, S. R., Silvano, A., Pena-Molino, B., van Wijk, E., Rosenberg, M., Greenbaum, J. S., and Blankenship, D. D.: Ocean heat drives rapid basal melt of the Totten Ice Shelf, *Science Advances*, 2, <https://doi.org/10.1126/sciadv.1601610>, 2016.

Roquet, F., Wunsch, C., Forget, G., Heimbach, P., Guinet, C., Reverdin, G., Charrassin, J., Bailleul, F., Costa, D. P., Huckstadt, L. A., Goetz, K. T., Kovacs, K. M., Lydersen, C., Biuw, M., Nøst, O. A., Bornemann, H., Ploetz, J., Bester, M. N., McIntyre, T., Muelbert, M. C., Hindell, M. A., McMahon, C. R., Williams, G., Harcourt, R., Field, I. C., Chafik, L., Nicholls, K. W., Boehme, L., and Fedak, 1130 M. A.: Estimates of the Southern Ocean general circulation improved by animal-borne instruments, *Geophysical Research Letters*, 40, 6176–6180, <https://doi.org/10.1002/2013gl058304>, 2013.

Roquet, F., Williams, G., Hindell, M. A., Harcourt, R., McMahon, C., Guinet, C., Charrassin, J.-B., Reverdin, G., Boehme, L., Lovell, P., and Fedak, M.: A Southern Indian Ocean database of hydrographic profiles obtained with instrumented elephant seals, *Scientific Data*, 1, <https://doi.org/10.1038/sdata.2014.28>, 2014.

1135 Rugenstein, M., Stocchi, P., von der Heydt, A., Dijkstra, H., and Brinkhuis, H.: Emplacement of Antarctic ice sheet mass affects circumpolar ocean flow, *Global and Planetary Change*, 118, 16–24, <https://doi.org/10.1016/j.gloplacha.2014.03.011>, 2014.

Rydt, J. D. and Gudmundsson, G. H.: Coupled ice shelf-ocean modeling and complex grounding line retreat from a seabed ridge, *Journal of Geophysical Research: Earth Surface*, 121, 865–880, <https://doi.org/10.1002/2015jf003791>, 2016.

Scheinert, M., Buchta, E., King, M., Wilson, T., Gomez, D., Kendrick, E., Koulali, A., Clarke, P., and Knöfel, C.: Reprocessing of geodetic 1140 GNSS recordings in Antarctica for geodetic and geodynamic applications (GIANT-REGAIN), in: General Assembly of the International Union of Geodesy and Geophysics (IUGG), GFZ German Research Centre for Geosciences, <https://doi.org/10.57757/IUGG23-3431>, 2023.

Schmidtko, S., Heywood, K. J., Thompson, A. F., and Aoki, S.: Multidecadal warming of Antarctic waters, *Science*, 346, 1227–1231, <https://doi.org/10.1126/science.1256117>, 2014.

Seroussi, H., Nowicki, S., Payne, A. J., Goelzer, H., Lipscomb, W. H., Abe-Ouchi, A., Agosta, C., Albrecht, T., Asay-Davis, X., Barthel, 1145 A., Calov, R., Cullather, R., Dumas, C., Galton-Fenzi, B. K., Gladstone, R., Golledge, N. R., Gregory, J. M., Greve, R., Hattermann, T., Hoffman, M. J., Humbert, A., Huybrechts, P., Jourdain, N. C., Kleiner, T., Larour, E., Leguy, G. R., Lowry, D. P., Little, C. M., Morlighem, M., Pattyn, F., Pelle, T., Price, S. F., Quiquet, A., Reese, R., Schlegel, N.-J., Shepherd, A., Simon, E., Smith, R. S., Straneo, F., Sun, S., Trusel, L. D., Van Breedam, J., van de Wal, R. S. W., Winkelmann, R., Zhao, C., Zhang, T., and Zwinger, T.: ISMIP6 Antarctica: a multi- 1150 model ensemble of the Antarctic ice sheet evolution over the 21st century, *The Cryosphere*, 14, 3033–3070, <https://doi.org/10.5194/tc-14-3033-2020>, 2020.

Shepherd, A., Ivins, E. R., A, G., Barletta, V. R., Bentley, M. J., Bettadpur, S., Briggs, K. H., Bromwich, D. H., Forsberg, R., Galin, N., Horwath, M., Jacobs, S., Joughin, I., King, M. A., Lenaerts, J. T. M., Li, J., Ligtenberg, S. R. M., Luckman, A., Luthcke, S. B., McMillan, 1155 M., Meister, R., Milne, G., Mouginot, J., Muir, A., Nicolas, J. P., Paden, J., Payne, A. J., Pritchard, H., Rignot, E., Rott, H., Sørensen, L. S., Scambos, T. A., Scheuchl, B., Schrama, E. J. O., Smith, B., Sundal, A. V., van Angelen, J. H., van de Berg, W. J., van den Broeke, M. R., Vaughan, D. G., Velicogna, I., Wahr, J., Whitehouse, P. L., Wingham, D. J., Yi, D., Young, D., and Zwally, H. J.: A Reconciled Estimate of Ice-Sheet Mass Balance, *Science*, 338, 1183–1189, <https://doi.org/10.1126/science.1228102>, 2012.

Stuhne, G. R. and Peltier, W. R.: Reconciling the ICE-6G\_C reconstruction of glacial chronology with ice sheet dynamics: The cases of Greenland and Antarctica, *Journal of Geophysical Research: Earth Surface*, 120, 1841–1865, <https://doi.org/10.1002/2015jf003580>, 2015.

Sun, C., Liu, C., Wang, Z., Yan, L., Tao, Y., Qin, Q., and Qian, J.: On the influences of the continental shelf bathymetry correction in Prydz Bay, East Antarctica, *Frontiers in Marine Science*, 9, <https://doi.org/10.3389/fmars.2022.957414>, 2022.

The ISMIP6 2300 extension authors: ISMIP6 Projections 2300 Antarctica, <https://thegithub.org/groups/ismip6/wiki/ISMIP6-Projections2300-Antarctica>, Last accessed July 25, 2023, 2022.

Thoma, M., Jenkins, A., Holland, D., and Jacobs, S.: Modelling Circumpolar Deep Water intrusions on the Amundsen Sea continental shelf, 1160 Antarctica, *Geophysical Research Letters*, 35, <https://doi.org/10.1029/2008gl034939>, 2008.

Thompson, A. F., Stewart, A. L., Spence, P., and Heywood, K. J.: The Antarctic Slope Current in a Changing Climate, *Reviews of Geophysics*, 56, 741–770, <https://doi.org/10.1029/2018rg000624>, 2018.

Tinto, K. J., Padman, L., Siddoway, C. S., Springer, S. R., Fricker, H. A., Das, I., Caratori Tontini, F., Porter, D. F., Frearson, N. P., Howard, 1170 S. L., Siegfried, M. R., Mosbeux, C., Becker, M. K., Bertinato, C., Boghosian, A., Brady, N., Burton, B. L., Chu, W., Cordero, S. I., Dhakal, T., Dong, L., Gustafson, C. D., Keeshin, S., Locke, C., Lockett, A., O'Brien, G., Spergel, J. J., Starke, S. E., Tankersley, M., Wearing, M. G., and Bell, R. E.: Ross Ice Shelf response to climate driven by the tectonic imprint on seafloor bathymetry, *Nature Geoscience*, 12, 441–449, <https://doi.org/10.1038/s41561-019-0370-2>, 2019.

Treasure, A., Roquet, F., Ansorge, I., Bester, M., Boehme, L., Bornemann, H., Charrassin, J.-B., Chevallier, D., Costa, D., Fedak, M., Guinet, C., Hammill, M., Harcourt, R., Hindell, M., Kovacs, K., Lea, M.-A., Lovell, P., Lowther, A., Lydersen, C., McIntyre, T., McMahon, C.,

1175 Muelbert, M., Nicholls, K., Picard, B., Reverdin, G., Trites, A., Williams, G., and de Bruyn, P. N.: Marine Mammals Exploring the Oceans Pole to Pole: A Review of the MEOP Consortium, *Oceanography*, 30, 132–138, <https://doi.org/10.5670/oceanog.2017.234>, 2017.

van Calcar, C. J., van de Wal, R. S. W., Blank, B., de Boer, B., and van der Wal, W.: Simulation of a fully coupled 3D glacial isostatic adjustment – ice sheet model for the Antarctic ice sheet over a glacial cycle, *Geoscientific Model Development*, 16, 5473–5492, <https://doi.org/10.5194/gmd-16-5473-2023>, 2023.

1180 Whitehouse, P. L.: Glacial isostatic adjustment modelling: historical perspectives, recent advances, and future directions, *Earth Surface Dynamics*, 6, 401–429, <https://doi.org/10.5194/esurf-6-401-2018>, 2018.

Whitehouse, P. L., Gomez, N., King, M. A., and Wiens, D. A.: Solid Earth change and the evolution of the Antarctic Ice Sheet, *Nature Communications*, 10, <https://doi.org/10.1038/s41467-018-08068-y>, 2019.

Wilmes, S., Green, J. A. M., Gomez, N., Rippeth, T. P., and Lau, H.: Global Tidal Impacts of Large-Scale Ice Sheet Collapses, *Journal of Geophysical Research: Oceans*, 122, 8354–8370, <https://doi.org/10.1002/2017jc013109>, 2017.

1185 Winkelmann, R., Martin, M. A., Haseloff, M., Albrecht, T., Bueler, E., Khroulev, C., and Levermann, A.: The Potsdam Parallel Ice Sheet Model (PISM-PIK) – Part 1: Model description, *The Cryosphere*, 5, 715–726, <https://doi.org/10.5194/tc-5-715-2011>, 2011.

Yokoyama, Y., Esat, T. M., Thompson, W. G., Thomas, A. L., Webster, J. M., Miyairi, Y., Sawada, C., Aze, T., Matsuzaki, H., Okuno, J., Fallon, S., Braga, J.-C., Humblet, M., Iryu, Y., Potts, D. C., Fujita, K., Suzuki, A., and Kan, H.: Rapid glaciation and a two-step sea level plunge into the Last Glacial Maximum, *Nature*, 559, 603–607, <https://doi.org/10.1038/s41586-018-0335-4>, 2018.

1190 Zeitz, M., Haacker, J. M., Donges, J. F., Albrecht, T., and Winkelmann, R.: Dynamic regimes of the Greenland Ice Sheet emerging from interacting melt–elevation and glacial isostatic adjustment feedbacks, *Earth System Dynamics*, 13, 1077–1096, <https://doi.org/10.5194/esd-13-1077-2022>, 2022.

Zwally, H. J., Giovinetto, M. B., Beckley, M. A., and Saba, J. L.: Antarctic and Greenland Drainage Systems [Dataset], <http://imbie.org/imbie-3/drainage-basins/>, accessed 27 November 2018, 2012.

1195 Zweng, M., Reagan, J., Seidov, D., Boyer, T., Locarnini, M., Garcia, H., Mishonov, A., Baranova, O., Weathers, K., Paver, C., and Smolyar, I.: World Ocean Atlas 2018, Volume 2: Salinity, Report, [https://data.nodc.noaa.gov/woa/WOA18/DOC/woa18\\_vol2.pdf](https://data.nodc.noaa.gov/woa/WOA18/DOC/woa18_vol2.pdf), 2019.

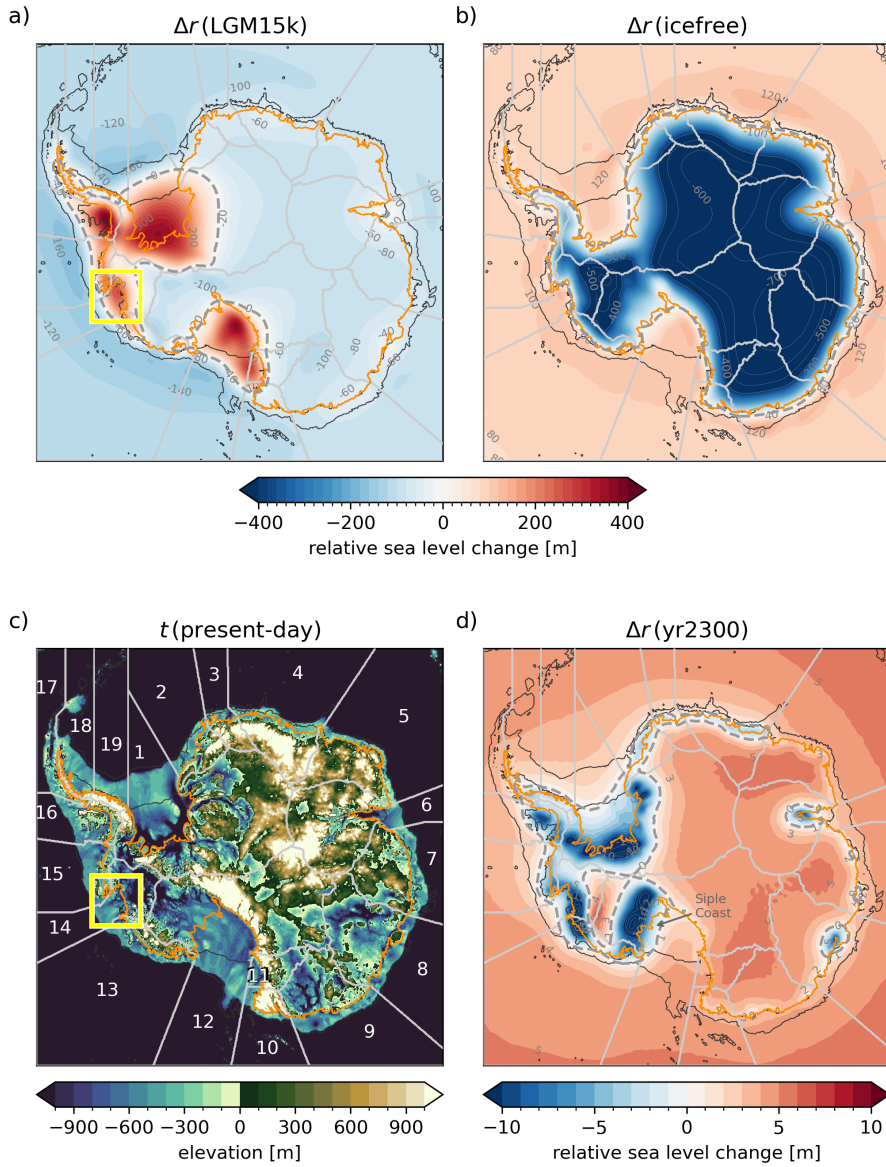


**Figure 2. Changes in relative sea-level for different scenarios and present-day topography.** Relative sea-level changes for different configurations and present-day topography. Changes in relative sea level  $\Delta r$  are shown for *LGM15k* (a), *icefree* (b) and *yr2300* (d) scenarios. The transition between positive and negative relative sea-level changes is indicated by thick dashed grey contour lines. Horizontally adjusted The grounding lines are shown in gold/orange and the present-day continental shelf corresponding continental-shelf area (excluding floating ice confined by continental-shelf break and present-day ice mask) is marked with black contour lines. Present-day reference topography  $t_{pd}$  (BedMachine v3) including basin numbers is shown in panel (c). Yellow and magenta rectangles indicate The yellow rectangle indicates the Amundsen Sea, (see Fig. 4, and Totten region, see Fig. ??, respectively.

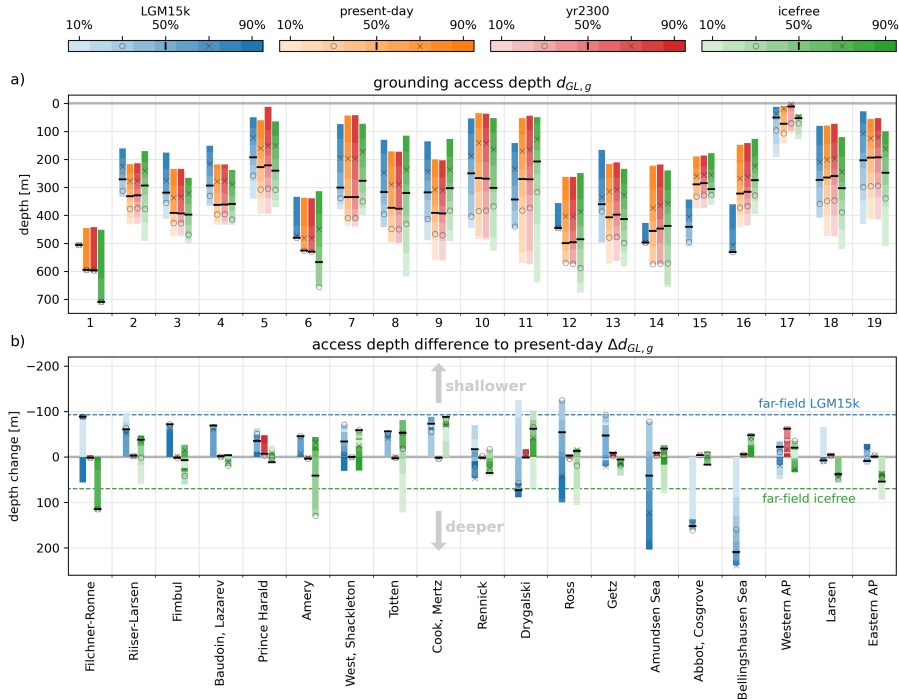


**Figure 3. Critical access depths (a) and their changes compared to present-day (b). Grounding line access depths  $d_{GL,g}$  (a) and their changes compared to present-day  $\Delta d_{GL,g}$  (b).** The colour shade indicates the percentage of grounding line reached by the specific critical access depth, with additional marks at 30% for  $d_{GL,30}$  (o), 50%  $d_{GL,50}$  (–) and 70%  $d_{GL,70}$  (x). Barystatic sea-level changes are indicated by dashed horizontal lines in panel b) for LGM15k and icefree scenario RSL configuration. The plot shows results for the present-day sensitivity experiment set, which uses a present-day ice mask and grounding line position, but updated topography. Basins are labelled according to prominent ice shelves following [Nicola et al. \(2023b, subm.; with AP = Antarctic Peninsula\)](#) [Nicola et al. \(2023b, in discuss.; with AP = Antarctic Peninsula\)](#).

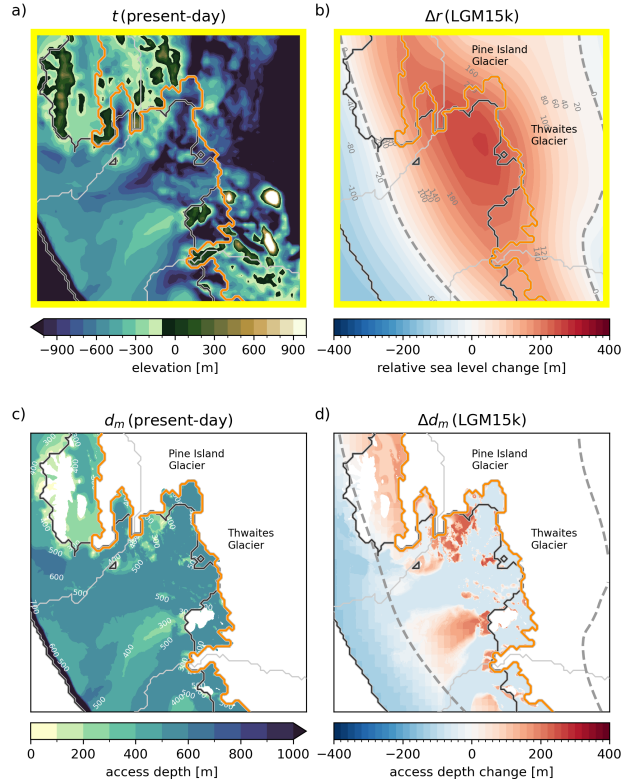
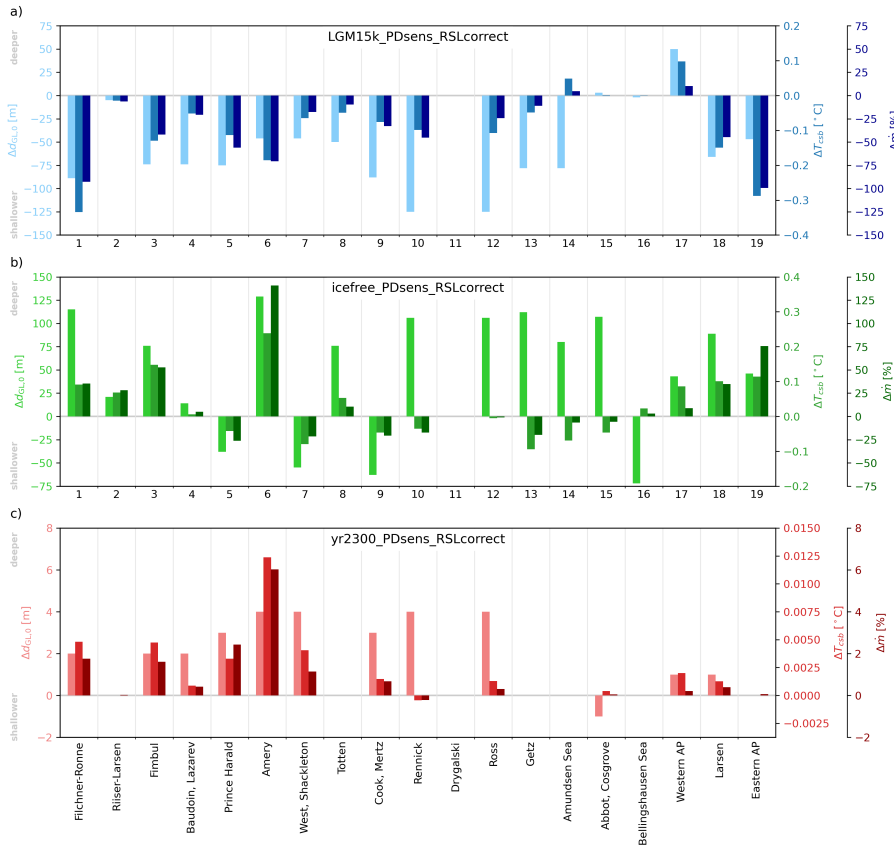


**Figure 4. Influence of relative sea-level change on critical access depths in the Amundsen Sea for the *LGM15k* scenario. Influence of relative sea-level change on access depths in the Amundsen Sea Embayment for the *LGM15k* RSL configuration.** Upper row shows present-day topography  $t_{pd}$  (a) and the change in relative sea level  $\Delta r$  in the *LGM15k* scenario configuration (b). Lower panels show the derived access depth map  $d_m$  for present-day bathymetry (c) and the corresponding change in the  $\Delta d_m$  for *LGM15k* scenario (d). Horizontally adjusted Present-day grounding line for present-day ice distribution is shown in orange and the present-day continental shelf area (excluding floating ice) is marked with black contour lines. The zero contour line of RSL changes is marked as a grey dashed line in panels b) and d). Yellow borders refer to map extent highlighted in Fig. 2.



#### Overview of derived critical access

**depths, ocean temperatures, salinities and basal melt rates for present-day conditions and their changes in the *LGM15k* and *icefree* scenarios.** Results are shown for all 19 Antarctic basins (see Fig. 2e) and grounding line coverage ranging from 10 to 90. Present-day melt rates are computed as in Reese et al. (2023) based on continental-shelf observations of ocean temperature and salinity. Displayed ranges for comparing *LGM15k* and *icefree* conditions to present-day are  $\pm 150$ ,  $\pm 0.8$  and  $\pm 0.15$  with exceeding values marked with purple and bright red colors respectively.

**Figure 5. Changes for grounding line access depth, ocean temperatures and basal melt rates (present-day sensitivity experiments).** The plot shows for each basin (from left to right): change in grounding line access depth ( $\Delta d_{GL,0}$ ), change in continental-shelf break temperature ( $\Delta T_{csb,mean}$ ) and relative change of basal melt rates ( $\Delta\dot{m}$ ) compared to baseline experiment PD\_baseline. Bar colors correspond to the respective y-axis. Note that the y-axis orientation for  $\Delta d_{GL,0}$  is reversed compared to Fig. 3 to be aligned with the orientation of  $\Delta T_{csb}$  and  $\Delta\dot{m}$ .

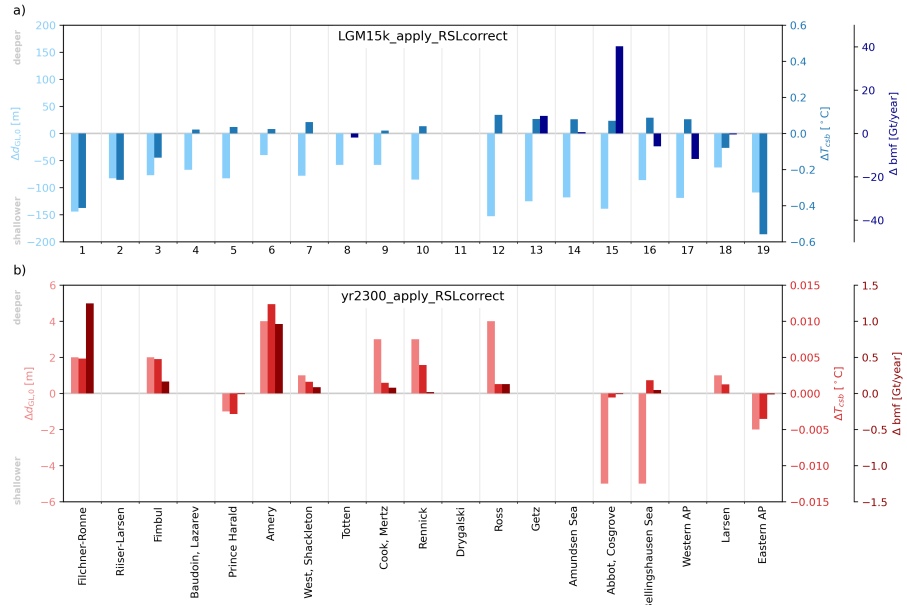


**Figure 6. Overview of critical access depth, ocean temperature, salinity and basal melt rate changes in the yr2300 scenario.** Results are shown for all 19 Antarctic basins (see [Changes for grounding line access depth, ocean temperatures and basal melt rates \(applied scenario experiments\)](#)). Similar to Fig. 2e-5, but anomalies are computed to LGM15k\_apply\_baseline and [grounding line coverage ranging from 10](#) yr2300\_apply\_baseline experiments, respectively. Other than in Fig. 5, changes in basal melting are displayed as absolute basal mass flux differences, which is more adequate as basal melting is close to 90 zero in many basins of LGM15k\_apply\_baseline.

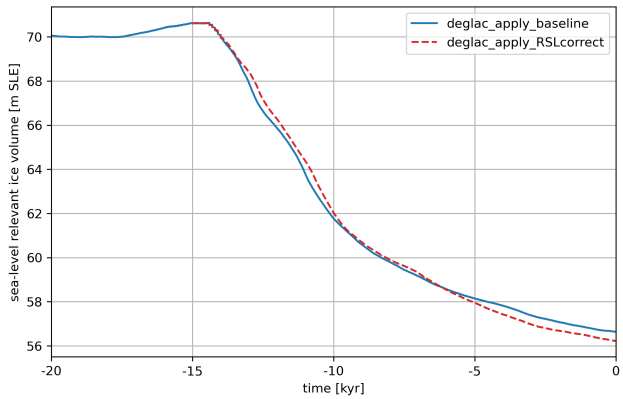


**Figure 7. Influence of RSL correction on the deglaciation of the Antarctic Ice Sheet.** m SLE = meter Sea Level Equivalent